Germanium enrichment in sphalerite with acicular and euhedral textures: an example from the Zhulingou carbonate-hosted Zn(-Ge) deposit, South China

Kai Luo, Alexandre Cugerone, Mei-Fu Zhou, Jia-Xi Zhou, Guo-Tao Sun, Jing Xu, Kang-Jian He, Mao-Da Lu

Mineralium Deposita
https://doi.org/10.1007/s00126-022-01112-4

ARTICLE

Germanium enrichment in sphalerite with acicular and euhedral textures: an example from the Zhulingou carbonate-hosted Zn(-Ge) deposit, South China

Kai Luo[1,2] · Alexandre Cugerone[3] · Mei-Fu Zhou[4] · Jia-Xi Zhou[1,2] · Guo-Tao Sun[5] · Jing Xu[6] · Kang-Jian He[7] · Mao-Da Lu[8]

Received: 27 April 2021 / Accepted: 31 March 2022

Abstract

Carbonate-hosted Pb–Zn deposits frequently contain significant amounts of critical metals such as germanium in sphalerite. However, the textural and chemical controls leading to Ge enrichment remain poorly constrained. Based on textural observations and laser-ablation (multi-collector) inductively coupled plasma mass spectrometry analysis, we investigate the origin, textural control, and incorporation of Ge in the Zhulingou carbonate-hosted Zn(-Ge) deposit, South China, which contains > 400t Ge at 97.9 ppm. Two hydrothermal stages (I and II) and three textural types of sphalerite (Sp1, Sp2, and Sp3) are recognized in stratabound and stockwork Zn(-Ge) orebodies. Acicular colloform Sp1 formed in stage I, whereas euhedral sector-zoned Sp3 is related to stage II. In acicular-euhedral Sp2, both Sp1 and Sp3 are observed. A large variation of Ge concentrations is observed with an average Ge of 1013 ppm in Sp1, decreasing to 621 ppm in Sp2 and to 492 ppm in Sp3. In the three types of sphalerite, Ge concentrations are not correlated to monovalent cations (Cu and Ag), indicative of unusual substitution mechanisms coupled to divalent cations such as Mn, Pb, or Cd. Trace element distribution, sulfur, and lead isotopes suggest that the deeply circulating brines interacted with Ge-rich basement rocks and mixed with shallow biogenic sulfur: This mixing process was certainly the main factor controlling the Ge endowment. The precipitation of acicular sphalerite was likely controlled by a combination of specific fluid conditions (i.e., low T and pH, and rapid mineral growth rate) and fluid mixing. These conditions leading to the formation of acicular sphalerite were favorable for Ge enrichment, compared to co-existing euhedral grains generally less rich in Ge.

Keywords Sphalerite · Germanium · LA-(MC)-ICP-MS analyses · Carbonate-hosted Zn(-Ge) deposits, South China

Introduction

Germanium is an important high-technology metal considered critical by the EU and USA due to its increasing use in fiber and infrared optics and polymerization catalysts (Schulz et al. 2017; European Commission 2020). It has a mean concentration of ~ 1.5 ppm in the continental crust (Smith and Huyck 1999) but may be found concentrated in various types of Zn-rich deposits, in trace concentrations (few hundreds of ppm Ge) (Höll et al. 2007; Sahlström

Editorial handling: S.-Y. Jiang

✉ Jia-Xi Zhou
zhoujiaxi@ynu.edu.cn

[1] School of Earth Sciences, Yunnan University, Kunming 650500, China

[2] Key Laboratory of Critical Minerals Metallogeny in Universities of Yunnan Province, Kunming 650500, China

[3] Department of Earth Sciences, University of Geneva, Geneva 1205, Switzerland

[4] State Key Laboratory of Ore Deposit Geochemistry, Institute of Geochemistry, Chinese Academy of Sciences, Guiyang 550081, China

[5] College of Resources and Environmental Engineering, Guizhou University, Guiyang 550025, China

[6] Zijin School of Geology and Mining , Fuzhou University, Fuzhou 350108, China

[7] School of Information Science and Engineering, Yunnan University, Kunming 650500, China

[8] Bureau of Geology and Mineral Exploration and Development of Guizhou Province, Duyun 558000, China

Published online: 18 April 2022

et al. 2017; Cugerone et al. 2018). Currently, Ge is mainly exploited as a by-product of mining and refining of Zn ores from carbonate-hosted Pb–Zn deposits (Gunn 2014; Licht et al. 2015; Mondillo et al. 2018).

Germanium is generally enriched in the sphalerite (ZnS) lattice (up to few thousands ppm Ge) and generally appears in the tetravalent oxidation state (Ge^{4+}) even if occasional divalent Ge^{2+} is reported (Bernstein 1985; Bélissont et al. 2016; Bonnet et al. 2017). Some authors inferred a coupled substitution with monovalent cations such as Cu to facilitate Ge incorporation in sphalerite ($Ge^{4+} + 2Cu^{+} \leftrightarrow 3Zn^{2+}$; e.g. Johan 1988; Ye et al. 2011; Bélissont et al. 2014, Cugerone et al. 2021). Other authors have suggested, based on the absence of correlation between Ge and other cations, that Ge substitutes directly for Zn^{2+} (e.g. Cook et al. 2009). Such examples include the presence of vacancies in the equation, such as $Ge^{4+} + (\text{vacancy}) \leftrightarrow 2Fe^{2+}$, and are likely more common in Fe-rich zones (Cook et al. 2015). Nonetheless, Hu et al. (2021) recently proposed unusual correlations between Ge, Mn, and Cd in Cu-poor sphalerite from the Huodehong deposit, South China. Based on these previous studies, Ge incorporation into sphalerite may occur via multiple substitution mechanisms, each probably related to local fluid conditions and compositions.

In carbonate-hosted Pb–Zn deposits, Ge is texturally controlled and concentrated in dark-brown zones of specific crystallographic faces of sphalerite (sector zoning or rhythmic bands; Bélissont et al. 2014; Bonnet et al. 2014; Cugerone et al. 2021). In poorly deformed environments, sphalerite crystals may have variable grain size and habits, from millimeter-size euhedral crystals to thin micrometer-sized acicular grains in colloform bands (Roedder 1968; Anderson 1975; Nakai et al. 1993; Barrie et al. 2009; Pfaff et al. 2011; Cook et al. 2015). In acicular crystals, the occurrence of wurtzite is inferred (hexagonal polytype of sphalerite) which is more enriched in Cu, Ag, and Sb compared to typical euhedral sphalerite (Beaudoin 2000; Pring et al. 2020). However, the distribution and control of critical metals such as Ge in these acicular crystals are still poorly known.

The origin of Ge enrichment in sphalerite is still debated between two different models, i.e. the control of low-temperature and high-salinity hydrothermal fluids (Frenzel et al. 2016; Bauer et al. 2019), or a direct link between adjacent rocks rich in Ge and high-grade Ge ores, such as differentiated granites or organic-rich sediments (Etschmann et al. 2017; Du et al. 2019).

The Zhulingou carbonate-hosted Ge-rich Zn deposit, South China, hosts various styles of Zn mineralization and sphalerite with euhedral and acicular textures, which provide a rare opportunity for a case study of the control and origin of Ge concentrations depending on sphalerite texture and related chemical conditions. The latest exploration in the Zhulingou deposit yielded 0.28 Mt Zn and > 400t Ge at grades of 6.5% Zn and 97.9 ppm Ge (Yang et al. 2020; Zhou et al. 2021). Such Ge grade and tonnage exceed those of most carbonate-hosted Pb–Zn deposits worldwide (10–100 ppm; e.g. Cook et al. 2009; Frenzel et al. 2014). The objective of this study is to understand the controls (such as temperature, sulfur fugacity, and pH) on textural heterogeneities (acicular and euhedral), chemical banding, and variable Ge concentrations. Understanding the cause of enrichment in Ge and related critical metals in sphalerite can provide valuable guidance in future exploration of Ge-rich deposits.

Regional geology

Tectonically, the Zhulingou deposit is located in the eastern part of the Yangtze Block, South China (Fig. 1a). The Yangtze Block is bounded by the Qinling-Dabie orogenic belt to the north, Tibetan plateau to the west, and the Cathaysia Block to the southeast (Fig. 1a; Zhou et al. 2002; Zhao et al. 2010; Gao et al. 2011). The eastern margin of the Yangtze Block is the Jiangnan orogenic belt, formed by the collision between the Yangtze Block and the Cathaysia Block at around 830 Ma (Zhao et al. 2011; Wu et al. 2022). The basement of the Yangtze Block is composed of late-Archaean metamorphic rocks and younger, weakly metamorphosed Mesoproterozoic to Neoproterozoic sedimentary successions including the Dongchuan, Huili, and Kunyang groups, all of which were intruded by widespread Neoproterozoic felsic to ultramafic rocks (Zhou et al. 2014; Hu et al. 2017). The sedimentary cover mainly consists of Paleozoic and Early-Mesozoic carbonate rocks with a local presence of sulfate evaporites with a shallow marine origin and Jurassic to Cenozoic continental clastic rocks (Yan et al. 2003; Zhou et al. 2018a).

A thousand carbonate-hosted Pb–Zn deposits are reported in the margins of the Yangtze Block and some of them are rich in Ge (Wen et al. 2019; Wu et al. 2019; Leach and Song 2019; Yang et al. 2021b). These deposits define the Sichuan-Yunnan-Guizhou (SYG) (Zhou et al. 2018b) and eastern Guizhou-western Hunan (EGWH) metallogenic belts (Fig. 1b; Wu et al. 2021; An et al. 2022). In the SYG belt, the closure of the Paleo-Tethys Ocean and the associated Indosinian Orogeny (257 ~ 200 Ma; Carter et al. 2001; Qiu et al. 2016) produced fault-fold systems that structurally controlled the occurrence of Pb–Zn deposits (Hu et al. 2017; Zhou et al. 2018c). These deposits include the world-class Huize deposit that contains > 7.0 Mt Pb + Zn, 4713 t Cd, and 525 t Ge (Ji 2019; Tao et al. 2019) and the Daliangzi deposit with 1.8 Mt Pb + Zn, 21,416 t Cd and 274 t Ge (Yuan et al. 2018; Tao et al. 2019).

In the EGWH belt, various tectonic events occurred after the amalgamation of the Yangtze Block and Cathysia Block in the Neoproterozoic and included the Nanhua rifting event (820 ~ 635 Ma), Caledonian shortening events

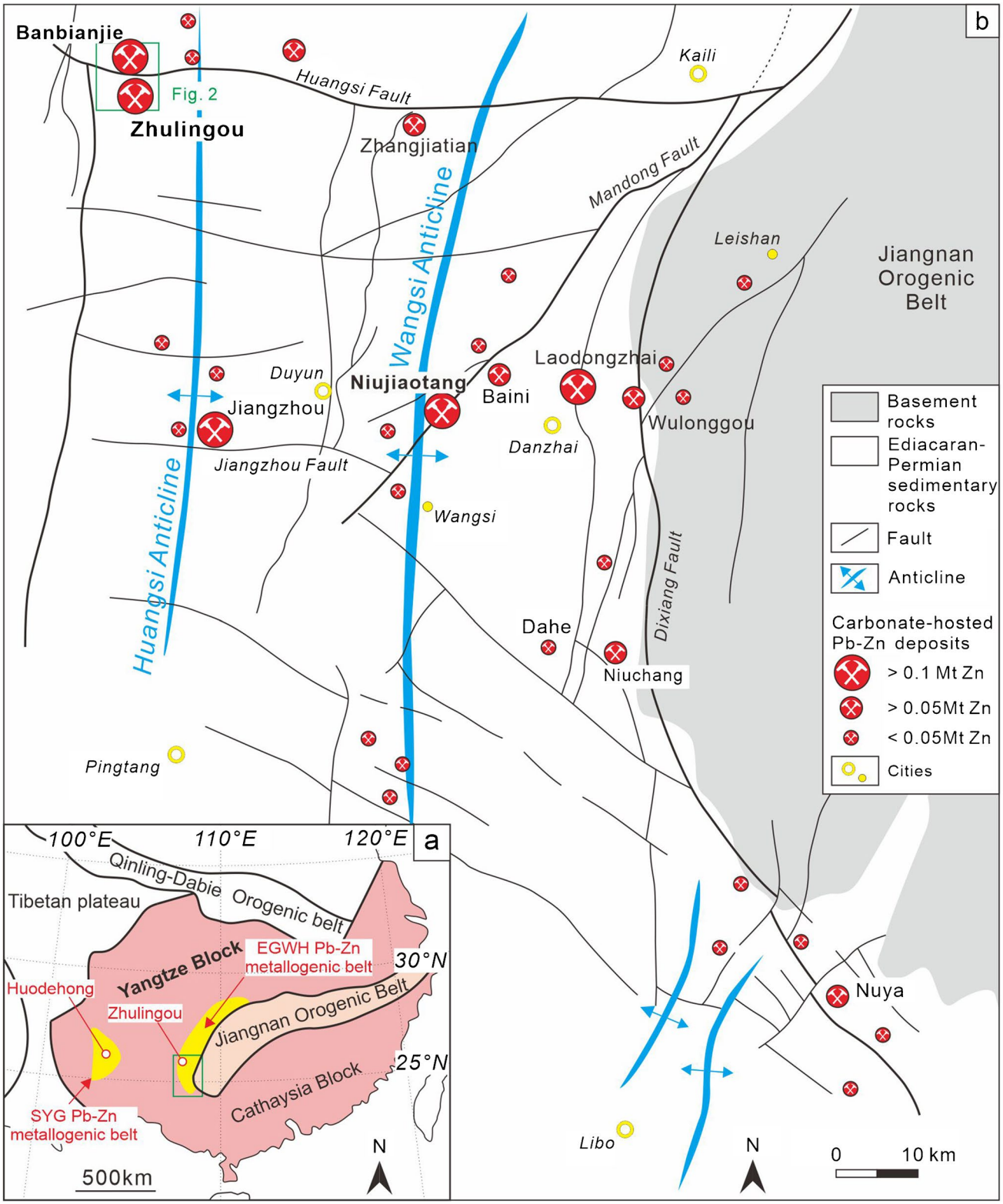

Fig. 1 (a) Simplified tectonic map of South China, showing the location of the study area in the eastern Guizhou and western Hunan (EGWH) carbonate-hosted Pb–Zn metallogenic belt. (b) Simplified geological map of the southwestern EGWH metallogenic belt representing the main geological structures and showing the location of the main carbonated-hosted Pb–Zn deposits in the area, including Zhulingou

(488 ~ 420 Ma) and finally, the Yanshanian intraplate activity (200 ~ 90 Ma) (Dai et al. 2015; Zhang et al. 2019). During the Caledonian orogenic events, NW-striking thrusting led to the uplift of the marginal fold belt, whereas NE-trending thrust faults and folds formed on the northwestern side of the Jiangnan orogeny belt (Ye et al. 2012). Moreover, the late NS-trending Jura-type folds are widely developed on the southeastern Yangtze Block, probably associated with the Yanshanian intraplate activity (Dai et al. 2015; An et al. 2022). In the northern part of the EGWH metallogenic belt, Pb–Zn mineralization is certainly genetically related to the Caledonian orogenic events (Zhou et al. 2016), whereas the Yanshanian orogenic event produced fault-fold systems that structurally controlled Pb–Zn deposits in the southwestern EGWH belt (Yang et al. 2021a). About 300 carbonate-hosted Pb–Zn deposits are reported in the EGWH belt, with an estimated total resource of > 20 Mt Pb + Zn (Wu et al. 2021). The EGWH belt extends for over 100 km in length and 20 km in width, and hosts the deposits of Danaopo (4.6 Mt Pb + Zn, 65,279 t Cd) (Wu et al. 2021), Niujiaotang (0.35 Mt Zn, 5300 t Cd) (Ye et al. 2012) and Banbianjie (0.80 Mt Zn, > 900t Ge) that is close to the Zhulingou deposit (Fig. 1b; Zhou et al. 2020). In these deposits, Pb–Zn orebodies are mostly stratabound and/or lenticular and are typically hosted within Ediacaran to Devonian dolostones or limestones (An et al. 2022). From east to west, there is a zonal distribution of deposits richer in Cu-Pb–Zn (Wulongou), Pb–Zn (Laodongzhai), Zn(-Cd) (Niujiaotang), to Zn(-Ge) (Banbianjie-Zhulingou) (Fig. 1b; Yang et al. 2017). These deposits are structurally controlled by brittle or ductile structures (fault and fold) or specific lithological interfaces. Brittle structures such as the E-W trending Huangsi and Jiangzhou, and the NE-trending Mandong faults are close to or directly host Pb–Zn mineralization.

Geology of the Zhulingou deposit

In the southwestern part of the EGWH metallogenic belt, the Banbianjie-Zhulingou carbonate-hosted Zn(-Ge) district (Fig. 1b) is composed of Cambrian to Permian sedimentary carbonate and clastic rocks (Fig. 2a). The Devonian Wangchengpo Formation hosts the main Zn(-Ge) mineralization and is composed of medium-grained bioclastic dolostones with vuggy structures and grey to greyish-white colors, and fine- to medium-grained siliceous dolostone with grey-black colors (Fig. 2b; Yang et al. 2020). The main Zn(-Ge) mineralization is spatially related to the late-Paleozoic Huangsi fault system with E-W to NNW-SSE-trending and moderate dipping (40–70°S; Fig. 2a). As an example, Fault F_1 trends N117°E with a sub-vertical dip of 70–85° to the NE and has an approximate offset of 65–70 m with a similar orientation to the main Huangsi fault. Important fault zones from 2 to 15 m in width are observed around the fault F_1 and conjugate F_2 fault. Nonetheless, at Zhulingou, mineralization seems to be essentially controlled by a lithological transition between carbonaceous mudstone and carbonate rocks. No primary genetic relationship between these faults and orebodies has been reported. However, Zn(-Ge) orebodies are thicker close to the fault systems, possibly implying that normal faults could be interpreted as a fluid migration pathway. Several reverse faults cut through the orebody and are post-mineralization (Fig. 3a).

The Zhulingou deposit is composed of three main orebodies I, II, and III depending on their locations with respect to the normal fault zones, F_1 and F_2 (Fig. 3a). Orebody I is located on the southwestern side (foot wall) of the F_1 fault, with an irregular thickness varying from 0.6 to 6.2 m and reaching a mean grade of 6.0% Zn. Orebody II is located on the northeastern side (hanging wall) of the fault F_1 and the southwestern side of the fault F_2, with variable thicknesses of 0.9–10.8 m, and a mean grade of 6.4% Zn. Orebody III occurs on the northern side of the F_2 fault with thicknesses varying from 0.5 to 16.3 m and a mean grade of 6.8% Zn. Germanium concentrations in ores have a large range between 35.2 and 174 ppm (mean 97.9 ppm) (Yang et al. 2020). The paragenetic sequence is relatively simple and dominantly composed of sphalerite (~ 60 vol %), and pyrite (~ 35 vol %) with minor marcasite and galena (~ 5 vol %). Gangue minerals are mainly dolomite, calcite, and quartz (Fig. 3b, c).

Analytical methods

Ninety-eight representative samples were collected from different parts of the three main orebodies, and in seven underground galleries (elevations reported in ESM 1). Forty-six polished sections containing sphalerite mineralization (150 µm thick) were studied.

Electron probe micro-analyses were carried out using a (JEOL) JXA8230 at the Wuhan Sample Solution Analytical Technology Co., Ltd, Hubei, China. Major, minor, and trace elements were measured with a beam current of 50 nA and an accelerating voltage of 15 kV. Zinc concentrations of sphalerite crystals were used as an internal calibration for LA-ICP-MS analyses.

LA-ICP-MS was used to determine minor and trace element concentrations of sphalerite. Both spot analyses and mapping were carried out, using a NWR ablation system ($\lambda = 193$ nm) coupled to an iCAP RQ ICP-MS instrument at Guangzhou Tuoyan Analytical Technology Co., Ltd., Guangzhou, China. Laser ablation was performed using a constant pulse rate of 10 Hz with a laser energy of 5 J/cm^2 and spot diameter of 30 µm. The following isotopes were quantified: ^{55}Mn, ^{57}Fe, ^{65}Cu, ^{71} Ga, ^{74}Ge, ^{75}As, ^{107}Ag, ^{111}Cd,

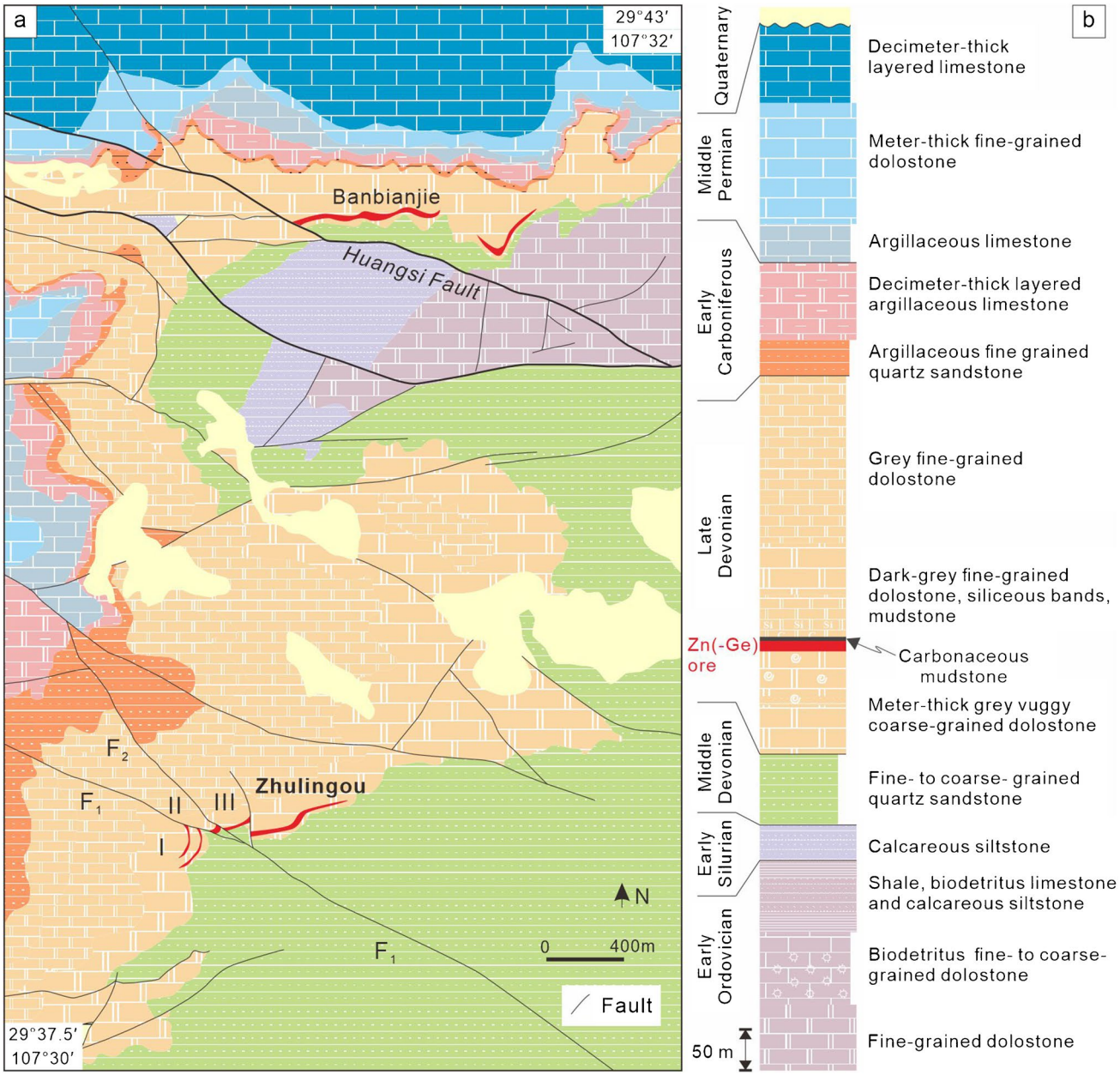

Fig. 2 (a) Geological map of the Zhulingou mining district. (b) Stratigraphic log in the Zhulingou-Banbianjie mining district, based on drill core logging and geological mapping

^{115}In, ^{118}Sn, ^{121}Sb, ^{202}Hg, and ^{208}Pb. Concentrations for ^{75}As, ^{118}Sn, ^{121}Sb, and ^{202}Hg were below the detection limit. Each analysis incorporated a background acquisition of 50 s followed by 40 s of sample data acquisition. NIST SRM 610 (Pearce et al. 1997) was used as an external standard. The MASS-1 sulfide reference material (57 ± 1.75 ppm value for Ge; Wilson et al. 2002) was used as a second external standard to identify possible instrumental drift. Data were processed using an Excel-based software Ilolite 3.6 (Paton et al. 2010) to perform off-line selection and integration of background and analyzed signals, time-drift correction, and quantitative calibration.

LA-ICP-MS elemental mapping was performed using the same laser ablation system with similar carrier gas settings as for spot analysis. Three selected areas of sphalerite grains were mapped using laser energy of 5 J/cm^2, a repetition rate of 20 Hz, 10 μm spot size, and stage translation speed of 20 μm/s. Background data was collected for 20 s at the beginning of each raster line. The data reduction was performed using Iolite 3.6.

a

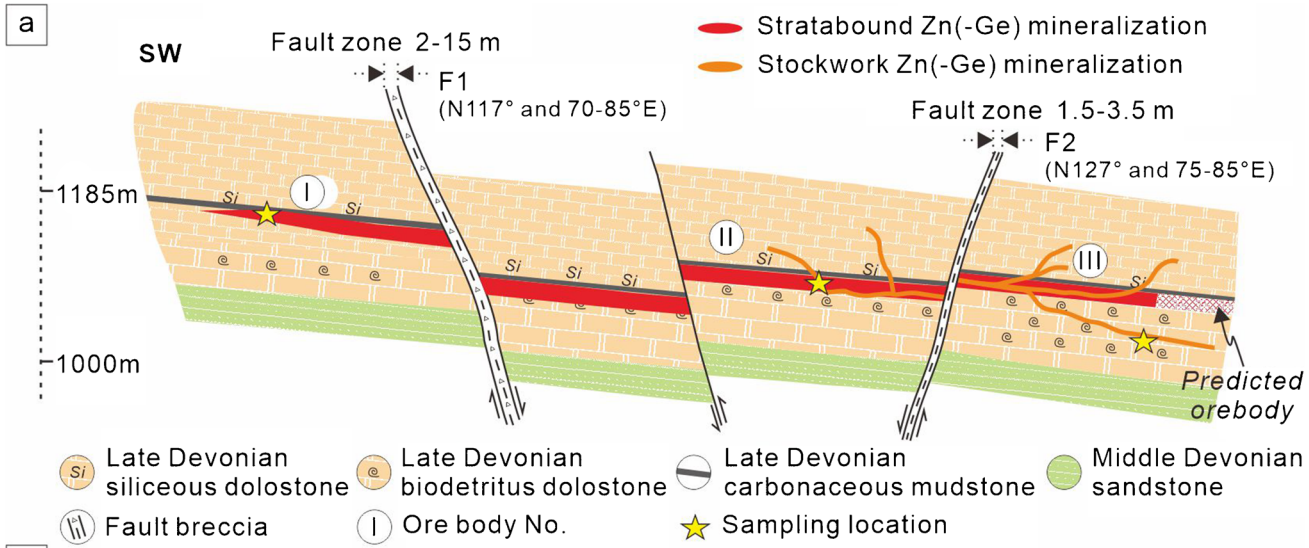

b

Min. type	Type 1 Statabound Brecciated	Type 2 Statabound Massive	Type 3 Stockwork
Host rock	Mainly dark-grey siliceous dolostone		Mainly light-grey biodetritus vuggy dolostone
Ore macro texture	Brecciated dolostone replaced by sulfides, fractured with dolomite infill	Massive vuggy sulfides coexisting with pyrite and black quartz	Pale yellow stockwork Sp and dolomite filling in fractures or replacing biodetritus of host rock
Zinc sulfide micro texture	Sp1: Yellow to dark-brown grains with acicular shape and frequently radial, cockade. Chemical banding with colloform textures/ fine-grained sphalerite disseminated in pyrite	Sp2: Yellow to dark-brown grains with acicular shape and frequently radial, cockade. Chemical banding with colloform textures/ infra millimeter-sized euhedral grains with light-brown color between layers of acicular sphalerite	Sp3: Coarse millimeter-sized light-yellow grains, local red sector zoning
Zonation	Opaque to light-brown oscillating bands (Clear laminae)	Opaque to light-brown oscillating bands (Blurred laminae)	Dark-brown sector zonings and light-brown domains
Assemblages	Sp1, Py1, Mc, (Gn)	Sp2, Py2	Sp3, Dol, (Py3)

c

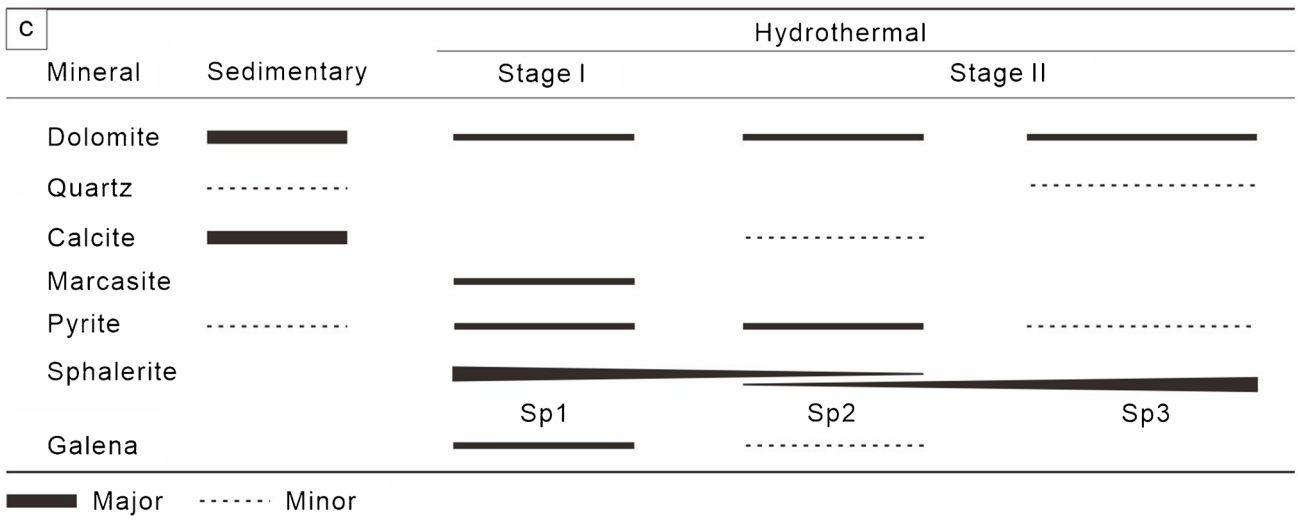

Fig. 3 (a) Simplified cross-section map of the Zhulingou Zn(-Ge) deposit, replacing the three mineralization types. (b) Main characteristics of the different mineralization types. (c) Mineral paragenesis of the Zhulingou Zn(-Ge) deposit

Mapping images were processed using the structural similarity index (SSIM) of images (Wang et al. 2004). MATLAB 7.0 software (Charbit 2010; see ESM 2 for detailed codes) was used to perform map calculation. The brightness, contrast, and structure of each map are broadly compared to estimate potential chemical correlation in estimating pixel intensity similarities between each map. If the SSIM had a relatively high value, the maps are considered similar, and therefore, the presence of correlations could be assumed. In contrast, if two elements were uncorrelated, the SSIM values would be relatively low.

In situ S isotope analyses of pyrite and sphalerite were conducted by LA-multi collector (MC)-ICP-MS at Nanjing FocuMS Technology Co. Ltd. The analyses were carried out using A Teledyne Cetac Technologies Analyte Excite laser-ablation system and Nu Instruments Nu Plasma II MC-ICP-MS. The 193 nm ArF excimer laser, homogenized by a set of beam delivery systems, was focused on the surface with a fluency of 2.5 J/cm^2. Each acquisition incorporated a 30-s background (gas blank) measurement, followed by 40 s of analysis with a spot diameter of 35 μm at a repetition rate 5 Hz. Natural Wenshan pyrite ($\delta^{34}S = +1.1‰$ V-CDT) was used as an external bracketing standard for each four analyses (Zhu et al. 2016). Pressed powder pellets of pyrite GBW07267 and chalcopyrite GBW07268 from National Research Center for Geoanalysis, China; Fu et al. 2016) with $\delta^{34}S$ values of +3.6‰ and -0.3‰, respectively, and fine-grained sphalerite SRM 123 with $\delta^{34}S$ value of +17.5‰, from the National Institute of Standards and Technology, USA (Craddock et al. 2008) were used to monitor analytical drift. The long-term reproducibility of $\delta^{34}S$ is better than 0.6‰ (one standard deviation).

In situ Pb isotope analyses of sulfide were performed on a Neptune Plus MC-ICP-MS equipped with a Geolas HD excimer ArF laser ablation system at the Wuhan Sample Solution Analytical Technology Co., Ltd, Hubei, China. The spot diameter ranged from 44 to 90 μm depending on Pb signal intensity. The pulse frequency ranged between 4 to 10 Hz, with a constant laser pulse intensity at ~ 5 J/cm^2. The isotopes ^{208}Pb, ^{207}Pb, ^{206}Pb, ^{204}Pb, ^{205}Tl, ^{203}Tl, and ^{202}Hg were collected in Faraday cups using static mode. Mass fractionation of Pb isotopes was corrected by ^{205}Tl/^{203}Tl with the exponential law. Optimized values of ^{205}Tl/^{203}Tl, were calibrated using the reference materials MASS-1 (USGS; Wilson et al. 2002) and Sph-HYLM (sphalerite; Feng et al. 2018). The ^{202}Hg signal was used to correct the remaining ^{204}Hg interference on ^{204}Pb, using the natural ^{202}Hg/^{204}Hg ratio (0.2301). In addition, the mass fractionation of ^{204}Hg/^{202}Hg was corrected by the ^{205}Tl/^{203}Tl normalization. Sph-HYLM was used to monitor the precision and accuracy of the measurements after ten sample analyses. The obtained accuracy is estimated to ± 0.2 ‰ for ^{208}Pb/^{204}Pb, ^{207}Pb/^{204}Pb, and ^{206}Pb/^{204}Pb compared to the solution value by MC-ICP-MS, with a typical precision of 0.4 ‰ (2σ). More detail of in situ Pb isotope ratio analysis can be found in Zhang et al. (2016). All data reduction for the MC-ICP-MS analysis of Pb isotope ratios was conducted using "Iso-Compass" software (Zhang et al. 2020).

Results

Mineralization types and sphalerite textures

At Zhulingou, there are three main types of Pb–Zn mineralization: (1) brecciated, (2) massive, and (3) stockwork. Each of these types has its own structures and sulfide textures (Fig. 4a–c). In these three types of mineralization, three types of sphalerite are observed, namely Sp1 (acicular; Fig. 4d-f), Sp2 (acicular-euhedral; Fig. 4g), and Sp3 (euhedral; Fig. 4h, i).

Type 1 stratabound brecciated mineralization

Type 1 mineralization is composed of brecciated ore with regular meter-thickness and with a general stratabound geometry (Fig. 5a). Brecciated ores are mostly constituted of sphalerite, pyrite, galena, and marcasite (60 vol % of sulfides) with local angular dolostone fragments (Fig. 4a). Large vugs are frequently observed and the silicified dolostone-host is cemented by sulfides (Fig. 4f). No syn-sedimentary evidence is reported, such as sulfide graded-beds or framboidal pyrite, and sulfide mineralization frequently crosscuts or replaces fossils such as *Temnophyllum* (Fig. 4e; Pedder 1972). These features clearly demonstrate that type 1 mineralization is epigenetic in origin. Sphalerite macrotexture appears commonly colloform, frequently associated with black organic matter (Fig. 5b), locally fractured and cemented by hydrothermal black fine-grained quartz (Fig. 4d). The main textural characteristic of Type 1 is acicular sphalerite crystals with pluri-micrometer thickness (Sp1) and up to few millimeters in length, commonly intergrown with fine-grained euhedral pyrite (Py1) and minor dendritic galena (Fig. 5c–f). There are locally late Sp3 veinlets that crosscut Py1 and Sp1 (Fig. 5c).

Under plane-polarized transmitted light, Sp1 is characterized by concentric millimeter oscillatory zoning with yellow to dark-brown colors (Fig. 6a), which exhibits generally planar, parallel, and locally sharp boundaries. Acicular crystals are commonly oriented perpendicular to the oscillatory zoning (Fig. 5e). Under crossed polarized transmitted light, anisotropic ZnS grains are observed in acicular sphalerite, (Fig. 6b), different from classical euhedral sphalerite crystals with isotropic extinction, which maybe induced by hexagonal ZnS (wurtzite; Pring et al. 2020). Nonetheless, XRD and Raman analyses could only confirm the occurrence of sphalerite (> 95%; see ESM 3; Zscheckel et al. 2016).

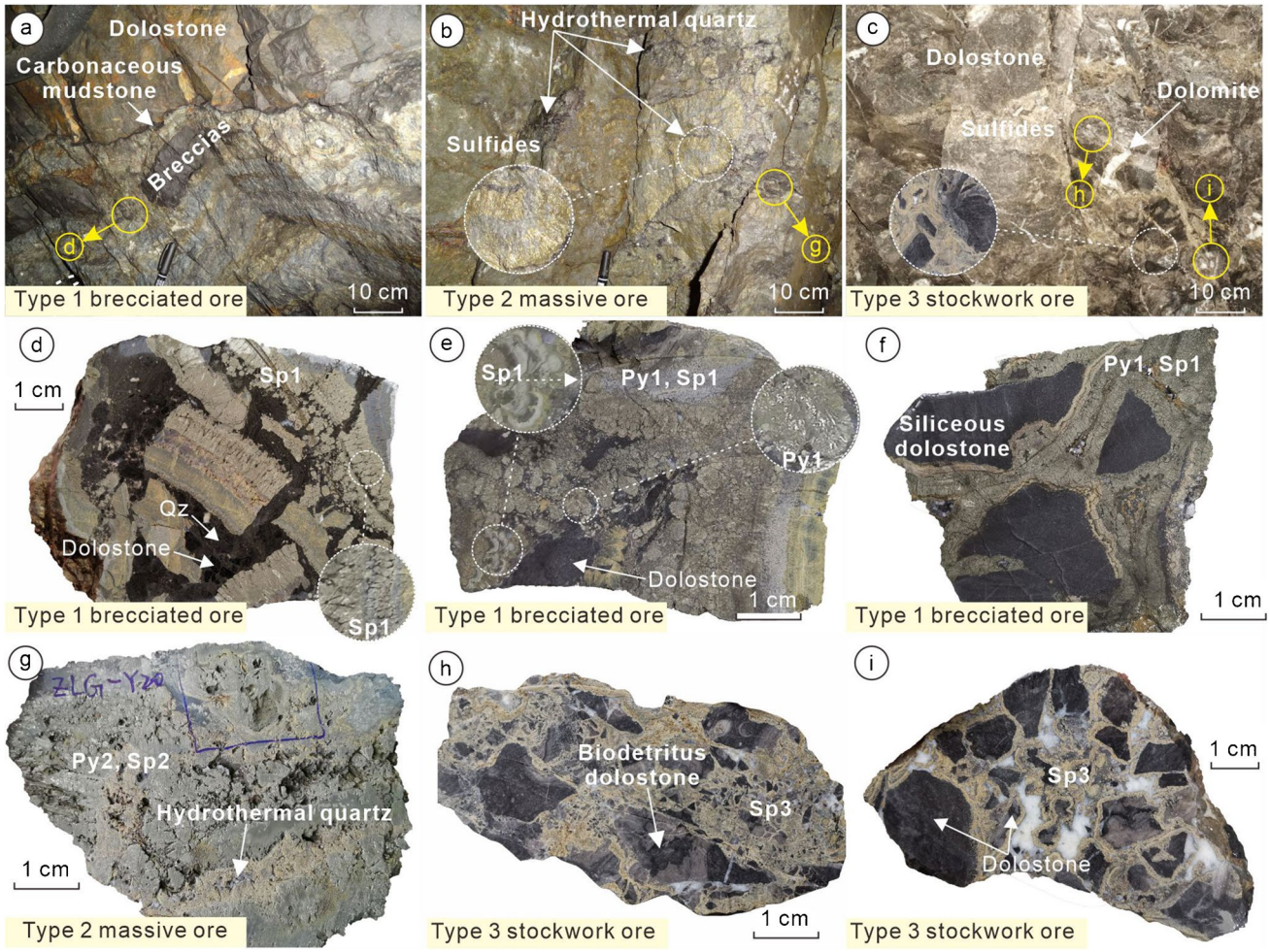

Fig. 4 Outcrop and rock specimen photographs of sulfide mineralization at Zhulingou. Locations of several samples are mentioned in a-c. (a) Type 1 brecciated sulfide mineralization hosted between black carbonaceous mudstone and dolostone. The yellow circle represents the location of the rock specimen. (b) Type 2 massive sulfide ores coexisting with black hydrothermal quartz (Qz). (c) Type 3 stockwork sulfides filling fractures of a bioclastic limestone. (d) Millimeter-sized acicular sphalerite (Sp1, see small inset) fractured and cemented by grey hydrothermal fine-grained quartz and black dolostone. (e) Organic-rich siliceous dolostones brecciated and selectively replaced by sulfides, showing colloform Sp1 (white dashed arrow indicates a direction of growth). Radial pyrite replaces the internal structures of cnidarian fossils. (f) Organic rich siliceous dolostones brecciated and cemented by acicular, colloform Sp1 and fine-grained euhedral pyrite (Py1). (g) Type 2 massive ore containing pyrite and colloform sphalerite with vugs filled with quartz and minor dolomite. (h, i) Type 3 stockwork sphalerite with light-yellow color filling fractures in biodetritus-rich dolostone

Type 2 stratabound massive mineralization

Type 2 mineralization is characterized by stratabound orebodies composed of massive ore with ~ 90 vol % sulfides (Fig. 4g), mostly of Sp2 and Py2, with hydrothermal, fine-grained quartz (< 10 µm), dolomite and calcite. Sulfides present evidence of local deformation, with rotation of sphalerite fragments and local heterogeneous grain size (Fig. 5g). Under plane-polarized transmitted light, Sp2 exhibits oscillatory light-yellow to dark-brown color bands that are concentric, and parallel but with gradational boundaries (Fig. 6c, d). The acicular grain texture similar to Sp1 is observed under crossed polarized transmitted light (Fig. 6d), but coarse and euhedral sphalerite (i.e., Sp3) layers also appear and are in close association with acicular sphalerite, preferentially in the light-yellow chemical zones (Fig. 6c). Dynamic recrystallization textures of sphalerite and probably pyrite and quartz are locally inferred with the occurrence of acicular-colloform sphalerite surrounded by fine-grained sphalerite (< 10–20 µm; Fig. 5e, f).

Type 3 stockwork mineralization

Type 3 stockwork mineralization is characterized by millimeter- to meter-thick veins with no preferential orientation, locally crosscutting type 1 stratabound ore (Figs. 4h, i and 5b, c). These veins are hosted in coarse-grained biodetritus dolostone with

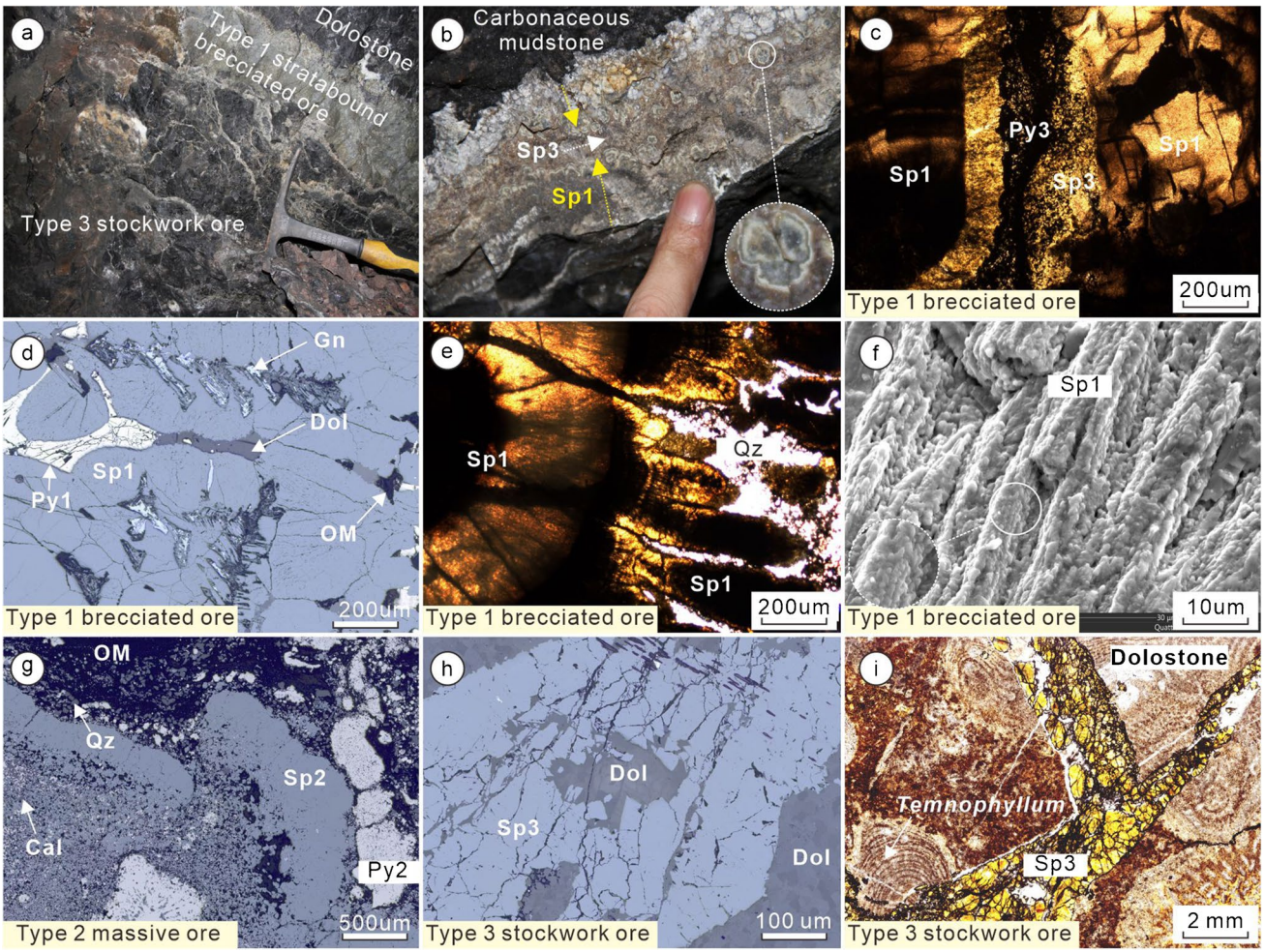

Fig. 5 Typical textures observed at Zhulingou. (a) Type 3 stockwork locally crosscutting type 1 stratabound orebodies. (b) Colloform sphalerite (Sp1) bodies with the local presence of euhedral Sp3 (white dashed arrow indicates a direction of growth). (c) Light-yellow fine-grained Sp3 and Py3 cross-cut light- to dark-brown Sp1 (transmitted plane-polarized light). (d) Association of Sp1 and dendritic galena with late pyrite grains (Py1) (reflected plane-polarized light). (e) Light-yellow to dark-brown colloform-like acicular sphalerite with leaf-shaped acicular sphalerite (transmitted plane-polarized light). (f) Sp1 with acicular shape and composed of nm-sized amorphous porous sphalerite (BSE image). (g) Sp2 with heterogeneous grain size, probably partly-recrystallized and coexisting with fine-grained calcite (reflected plane-polarized light). (h) Millimeter-sized grains of Sp3 coexisting with coarse-grained dolomite (Dol) (reflected plane-polarized light). (i) Sp3 stockwork crosscutting *Temnophyllum* fossils (reflected plane-polarized light)

occurrences of fragments of *Temnophyllum* (Pedder 1972), intensely fractured and partly associated with pyrite (Py3) and dolomite with pluri-millimeter grain size (Fig. 5h, i). In stockwork ore, euhedral sphalerite crystals (Sp3, up to 1 mm in size) with mostly light-yellow color dominate with generally no acicular texture (Fig. 6e, f). Locally, dark-brown millimeter-thick bands and sector zonings account for only up to 10% of each sphalerite crystal.

Chemical compositions of sphalerite

Quantitative LA-ICP-MS analyses of Sp1 ($n=29$), Sp2 ($n=28$), and Sp3 ($n=43$) are available in ESM 1 and were performed in sphalerite with various colors ranging from light-yellow to dark-brown, or from core to rim in concentric sphalerite structures. No Ge, Fe, or Pb micro-inclusions were observed in time-integrated LA-ICP-MS spectra, suggesting that measured elements may occur within the sphalerite lattice (ESM 3). Comparison of the shape of the time-integrated LA-ICP-MS spectra may show some trends between elements (ESM 3), as in the Sp2, where Ge is positively correlated with Fe, Pb, and/or Mn, whereas Ga is positively correlated with Cd.

Germanium contents decrease from Sp1 (770–1381 ppm, mean 1013 ppm), Sp2 (367–1174 ppm, mean 621 ppm), to Sp3 (276–818 ppm, mean 492 ppm). Iron contents of Sp1, Sp2, and Sp3 are relatively low with 1072–13,366 ppm (mean 5996 ppm), 2766–25,493 ppm (mean 9870 ppm), and 1715–18,700 ppm (mean 9336 ppm), respectively. Copper

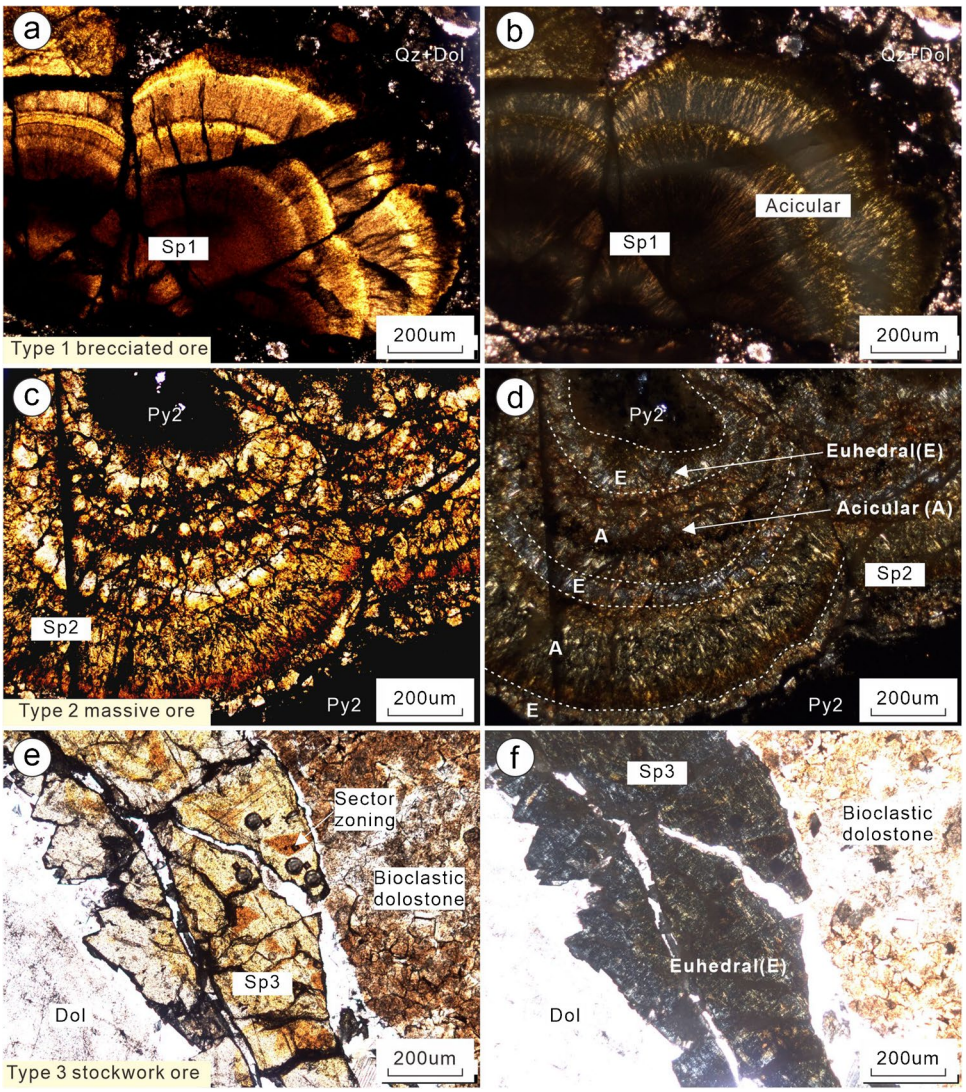

Fig. 6 Comparison of sphalerite types with acicular and euhedral textural observations in plane- and cross-polarized transmitted light. (a, b) Acicular and colloform Sp1, showing clear laminae of oscillating bands with light-yellow to dark-brown colors. The XRD and Raman results suggest that the acicular crystals are mostly sphalerite with no significant amount of wurtzite (ESM 3). (c, d) Acicular and euhedral Sp2 with colloform banding exhibiting light-yellow to dark-brown colors in acicular grains and quasi-only light-yellow colors in euhedral sphalerite (e, f) Light-yellow to brown Sp3 with sector zoning and locally rhythmic bands

concentrations in all three types of sphalerite are systematically low (0.2 to 8.4 ppm). Manganese, Ga, Ag, and Cd concentrations in Sp1, Sp2, and Sp3 range between 10.0 and 164 ppm, 1.46 and 139 ppm, 1.10 and 2.48 ppm, and 243 and 3243 ppm, respectively. Indium contents are negligible with concentrations below 0.3 ppm, whereas Pb concentrations vary from 210 to 9860 ppm.

Spatial distribution of Ge and related elements in sphalerite

Three representative maps of Sp1, Sp2, and Sp3 are shown in Figs. 7, 8, and 9. In Sp1, the main dark-brown band has high values of Mn, Ga, and Cd, and low Fe, Ge, and Pb (Fig. 7). The Ge-Mn, Ge-Fe, Ge-Cd, and Ge-Pb pairs have high and close affinity scores (SSIM) of 0.52, 0.49, 0.54, and 0.53, respectively (ESM 1 and ESM 3). On the Sp1 map, Ge concentrations seem broadly positively correlated with Pb and Fe (Fig. 7), whereas, Ge, Fe, and Pb are broadly negatively correlated with Cd concentration. In Sp1, Ga distribution is largely spread and is not clearly correlated with a particular element even if the highest concentrations are in the main dark-brown band, similar to Cd and Mn (Fig. 7).

In Sp2, a large discrepancy in chemical concentrations between acicular and euhedral sphalerite grains is observed. In coarse euhedral sphalerite with light-brown color, large depletions in Cd, Ge, Ga, Mn, and Pb are reported (Fig. 8). The darker brown Sp2 (i.e., mostly acicular sphalerite) is relatively rich in Cd, Ge, Mn and Pb. Moreover, close to the boundary between dark-brown and light-brown sphalerite, Ge and Mn have higher concentrations. The Ge-Mn, Ge-Cd, and Ge-Pb pairs have high affinity score (SSIM) of 0.66, 0.53 and 0.78, respectively. Low affinity scores are observed for Ge-Fe with 0.44 (ESM 1). Elemental mapping of Sp2 (Fig. 8) shows that Ge concentrations are positively correlated with Mn and broadly with Pb, and negatively correlated with Cd. Similarly, to Sp1, Ga concentrations covary positively with Cd in acicular sphalerite (Fig. 8).

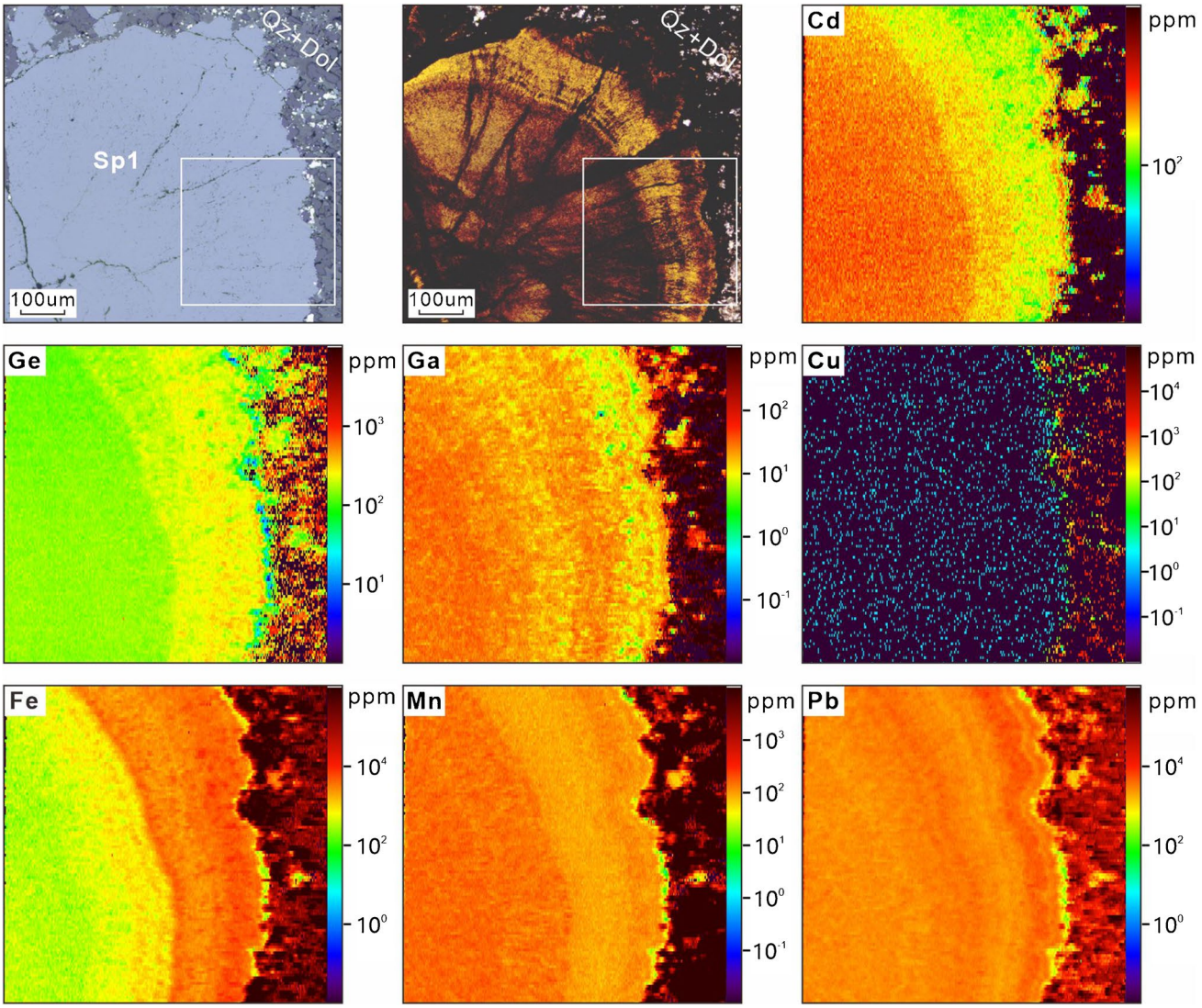

Fig. 7 LA-ICP-MS mapping images of type 1 brecciated, acicular and colloform-like sphalerite (Sp1), showing oscillating compositional and color zonings. Abbreviations: Qz-Quartz; Dol-Dolomite

In Sp3, complex zoning with dark-brown sectors and rhythmic bands have various chemical compositions. Sector zoning has relatively high Ge, Mn, and Pb concentrations as well as low Cd, Ga, and Fe (Fig. 9). Rhythmic bands are characterized by Cd concentrations in contrast to Ge, which does not display rhythmic band zoning (Fig. 9). Affinity scores (SSIM) between elemental pairs of Ge-Mn, Ge-Fe, Ge-Cd, and Ge-Pb, are 0.66, 0.61, 0.47, and 0.62, respectively. Elemental mapping of Sp3 (Fig. 9) shows that Ge is positively correlated with Mn and Pb. Germanium, Mn, and Pb are negatively correlated with Cd and covary with Fe. Gallium concentrations are positively correlated with Cd, especially in coarse sphalerite crystals (Fig. 9).

Sulfur isotope compositions

The sulfur isotope signatures of hydrothermal sphalerite (Sp1, Sp2, and Sp3; $n=29$) and pyrite (Py1 and Py2; $n=8$) were investigated (Fig. 10; ESM 1). Sulfides display a range of $\delta^{34}S$ values from −14.6 to −6.8‰. A general feature of these data is a trend from Sp1 to Sp3 with $\delta^{34}S_{Sp1}$ (−14.6 to −9.6‰; $n=18$) < $\delta^{34}S_{Sp2}$ (−9.2 to −6.8‰; $n=3$) ≈ $\delta^{34}S_{Sp3}$ (−8.7 to −7.5‰; $n=8$). In acicular Sp1 with oscillatory color zoning, $\delta^{34}S$ values (−11.5 to −9.7‰; $n=3$; Fig. 10a, b) have constant values in the core (−9 to −10‰) and lower values in the rim (−11‰) (Fig. 10d). Analyses of small anhedral Sp2 grains (−7.1 to −6.8‰; $n=3$) and co-existing coarse Py2

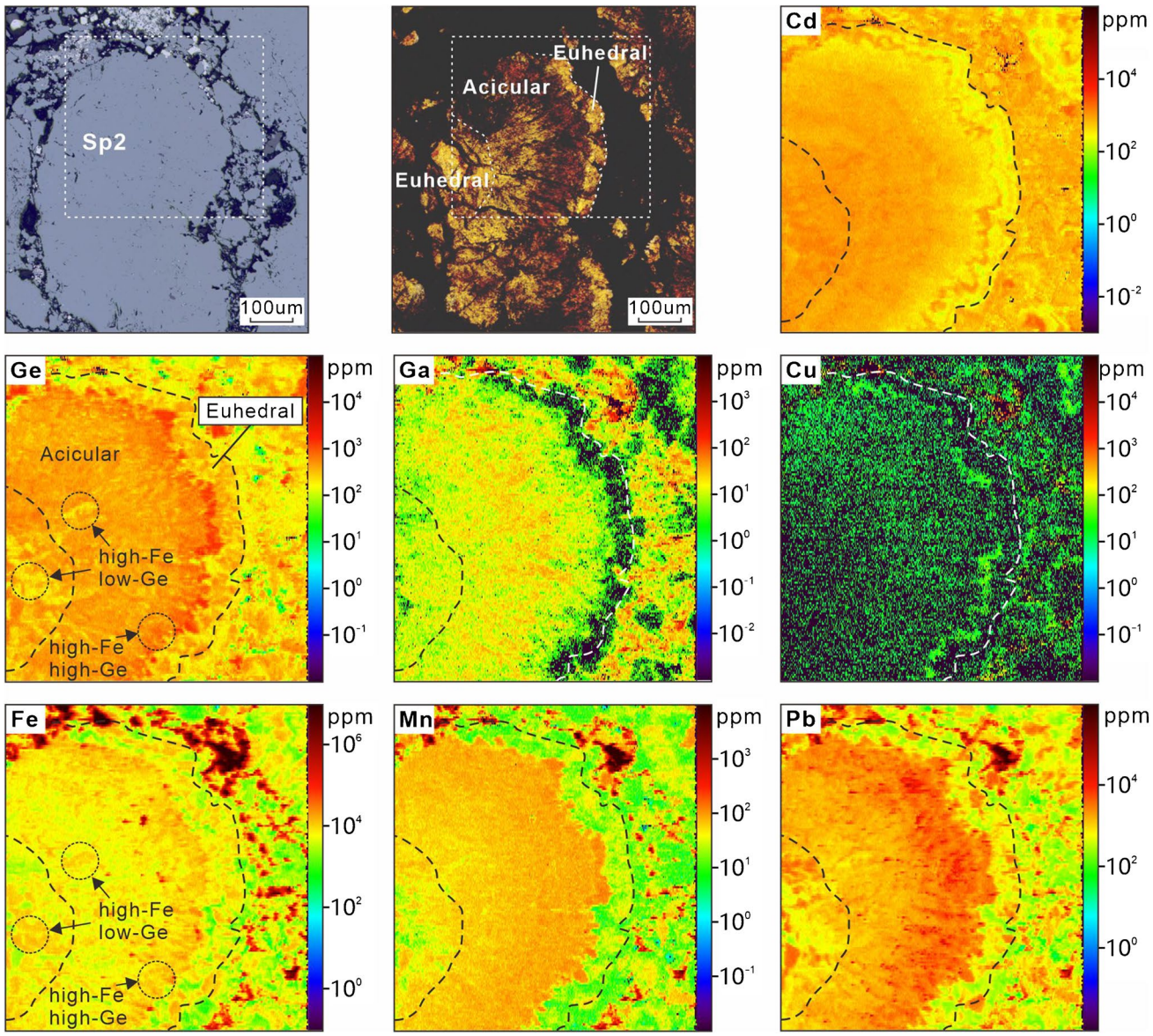

Fig. 8 LA-ICP-MS mapping images of type 2 massive sphalerite (Sp2), showing co-existence of acicular-euhedral sphalerite textures, with various oscillating compositional and color zones

(−9.2 to −9.1‰; $n=2$) indicate higher isotopic values in Py2-Sp2 than in Py1-Sp1 (Fig. 10e). In coarse-grained Sp3, $\delta^{34}S$ is homogeneous, ranging from −8.7 to −7.5‰ ($n=8$) (Fig. 10f), in which, red sectors have $\delta^{34}S$ values (−7.9 to −7.7‰) comparable with light-yellow domains (−8.7 to −7.5‰).

Lead isotope compositions

The Pb isotope systematics of hydrothermal Sp1-Py1, Sp2-Py2, and Sp3 were investigated in situ (Fig. 11; ESM 1). In Sp1, no significant difference in Pb isotope ratios is observed in a transect across acicular colloform Sp1 ($n=15$; Figs. 6a, b and 10a–c). In various Sp2 and Sp3 crystals, no significant Pb isotope ratio variations by color domains (dark and light; Fig. 10e, f) and with sphalerite grain size are observed. The main difference appears between Sp1 and Sp2-Sp3 (Fig. 11b). Sp1 displays relatively homogeneous and low Pb isotope ratios of $^{208}Pb/^{204}Pb = 38.06–38.09$, $^{207}Pb/^{204}Pb = 15.67–15.68$, $^{206}Pb/^{204}Pb = 18.13–18.15$ ($n=18$). Higher Pb isotope ratios are found in Sp2-Sp3 with $^{208}Pb/^{204}Pb$, $^{207}Pb/^{204}Pb$, and $^{206}Pb/^{204}Pb$ ratios of 38.12–38.19, 15.68–15.70, and 18.19–18.26, respectively ($n=15$). Py1 and Py2 have similar Pb isotope ratios with $^{208}Pb/^{204}Pb = 38.05–38.26$, $^{207}Pb/^{204}Pb = 15.67–15.72$, and $^{206}Pb/^{204}Pb = 18.13–18.32$ ($n=10$).

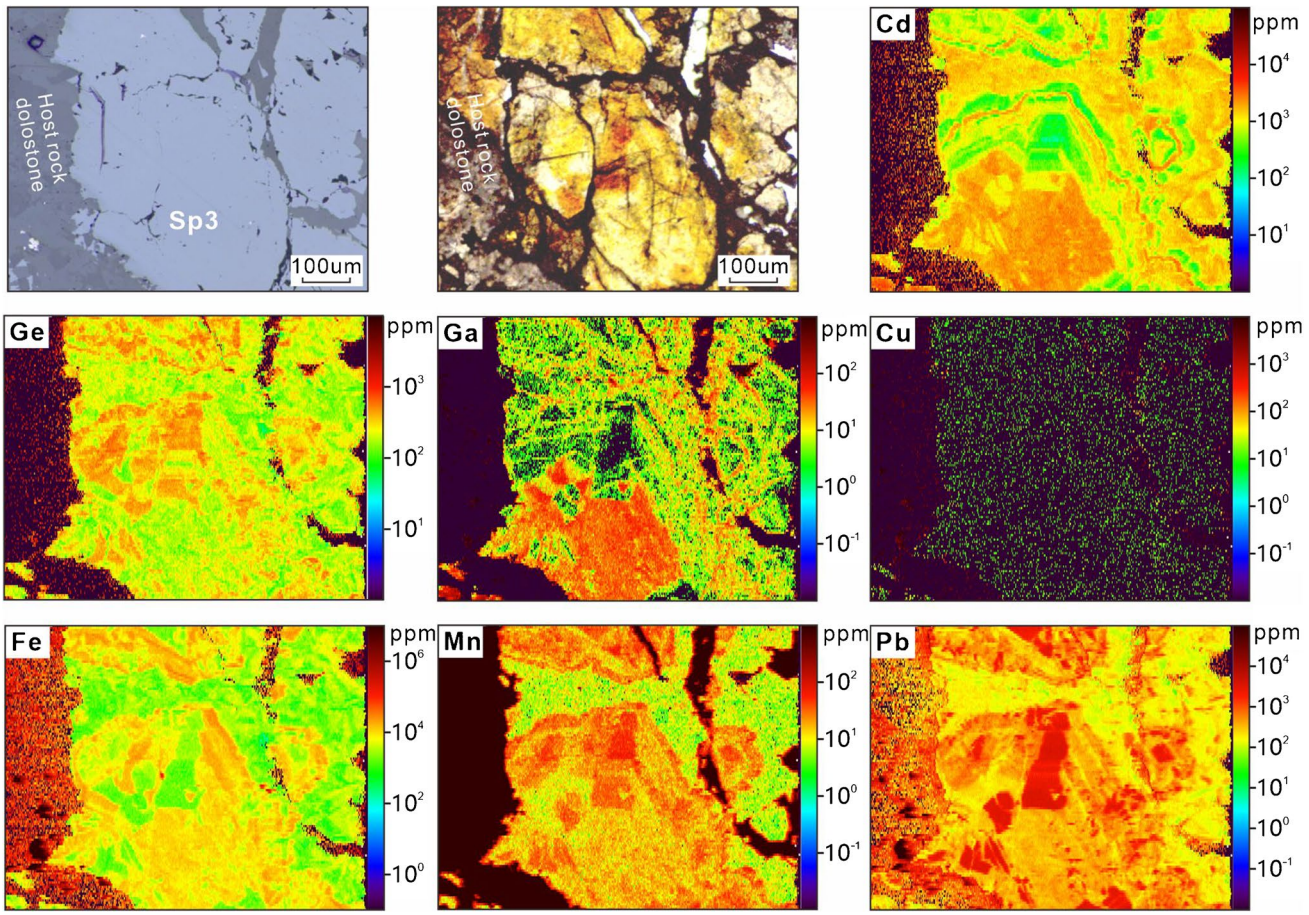

Fig. 9 LA-ICP-MS mapping images of type 3 stockwork sphalerite (Sp3), showing chemical distribution in sector zoning, rhythmic bands, and light color domains

Discussion

Acicular and euhedral sphalerite related to two mineralizing events.

At Zhulingou, detailed structural and textural observations unravel three types of epigenetic Zn-Ge ores, originating from two mineralizing events. Type 1 stratabound brecciated mineralization is mainly composed of sphalerite (Sp1) with acicular habit and with chemical oscillatory color bands. Substantial amount of fine-grained euhedral Py1 and dendritic galena are also found. These sulfides are in contact with thin bands of black organic matters.

Type 3 stockwork is a common carbonate-hosted mineralization with millimeter- to meter-thick veins with no preferential orientations and composed of zoned euhedral sphalerite (Sp3). These veins locally crosscut Sp1 and slightly post-date Ttype 1 stratabound breccia (Fig. 5a–c). Sulfur isotopic values show some differences between Sp1 and Sp3 with generally lower $\delta^{34}S$ values for Sp1 than Sp3 (Fig. 10). But in the same set of Sp1 grains, large variations in $\delta^{34}S$ values appear between core and rim (−9 to −11‰) which makes Sp1 $\delta^{34}S$ signature highly variable and locally close to Sp3 (Fig. 10d).

Type 2 stratabound massive mineralization shares significant structural and mineralogical similarities with Type 1, with the same orebody geometry and occurrence of acicular sphalerite, which likely infer an analogous origin for types 1 and 2. Nonetheless, type 2 mineralization is composed of both acicular Sp1 and coarse-euhedral Sp3 grain (both grouped in Sp2) as well as substantial amounts of fine sphalerite crystals (up to few tens of μm). Furthermore, Pb and S isotopic values show clear similarities between Sp2 and Sp3 (Fig. 11b). Trace element concentrations are also similar between Sp2 and Sp3 (i.e., Cd, Ge, Mn, Pb; Fig. 12), despite large discrepancies in the trace element distribution (Figs. 8 and 9). In Sp2, abundant deformation and probably recrystallization features are observed and related to post-mineralization deformation and close to the faults (Fig. 3a).

Therefore, we suggest the occurrence of two epigenetic mineralization events in the Zhulingou deposit (Fig. 3c). Hydrothermal stage I is characterized by the emplacement of

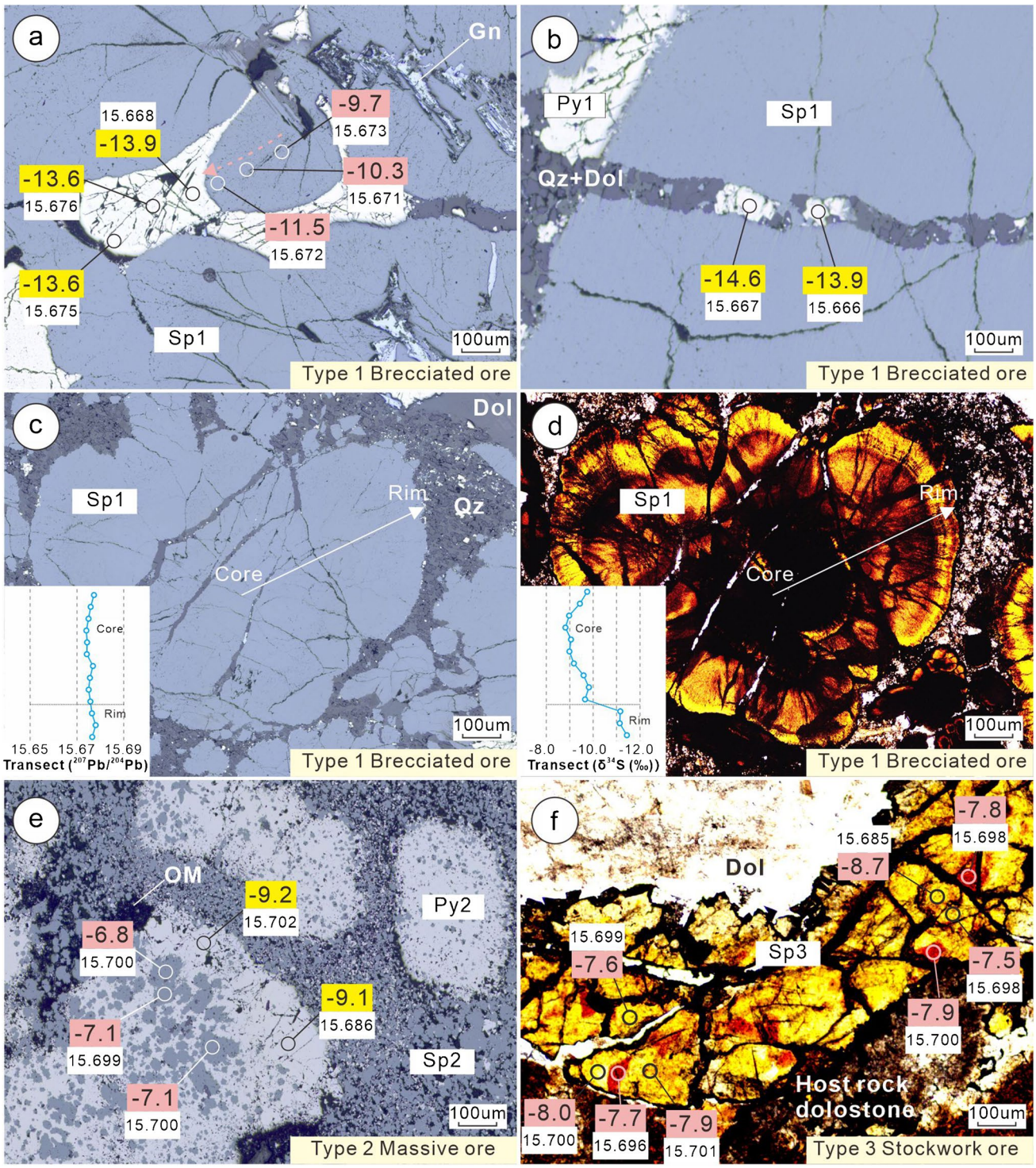

Fig. 10 Photomicrographs of sphalerite and pyrite from the Zhulingou Zn(-Ge) deposit, showing $\delta^{34}S$ and $^{207}Pb/^{204}Pb$ values for spots analyzed by LA-(MC)-ICPMS. (a–d) Sp1, with small graphs in (c) and (d) showing $^{207}Pb/^{204}Pb$ and $\delta^{34}S$ values, respectively; (e) Sp2 and complex textures with probable partly recrystallized sphalerite and pyrite; (f) Sp3 with similar S and Pb isotopic compositions in light-yellow and brown colors domains

stratabound-breccia mineralization, with acicular sphalerite (Sp1) texture. Following a gradual chemical evolution of the mineralizing fluids from stage I, the hydrothermal stage II is characterized by stockwork veins crosscutting dolostones or pre-existing type 1 mineralization. Stage II mainly precipitates Sp3 euhedral sphalerite. Sp2 ore certainly represents a

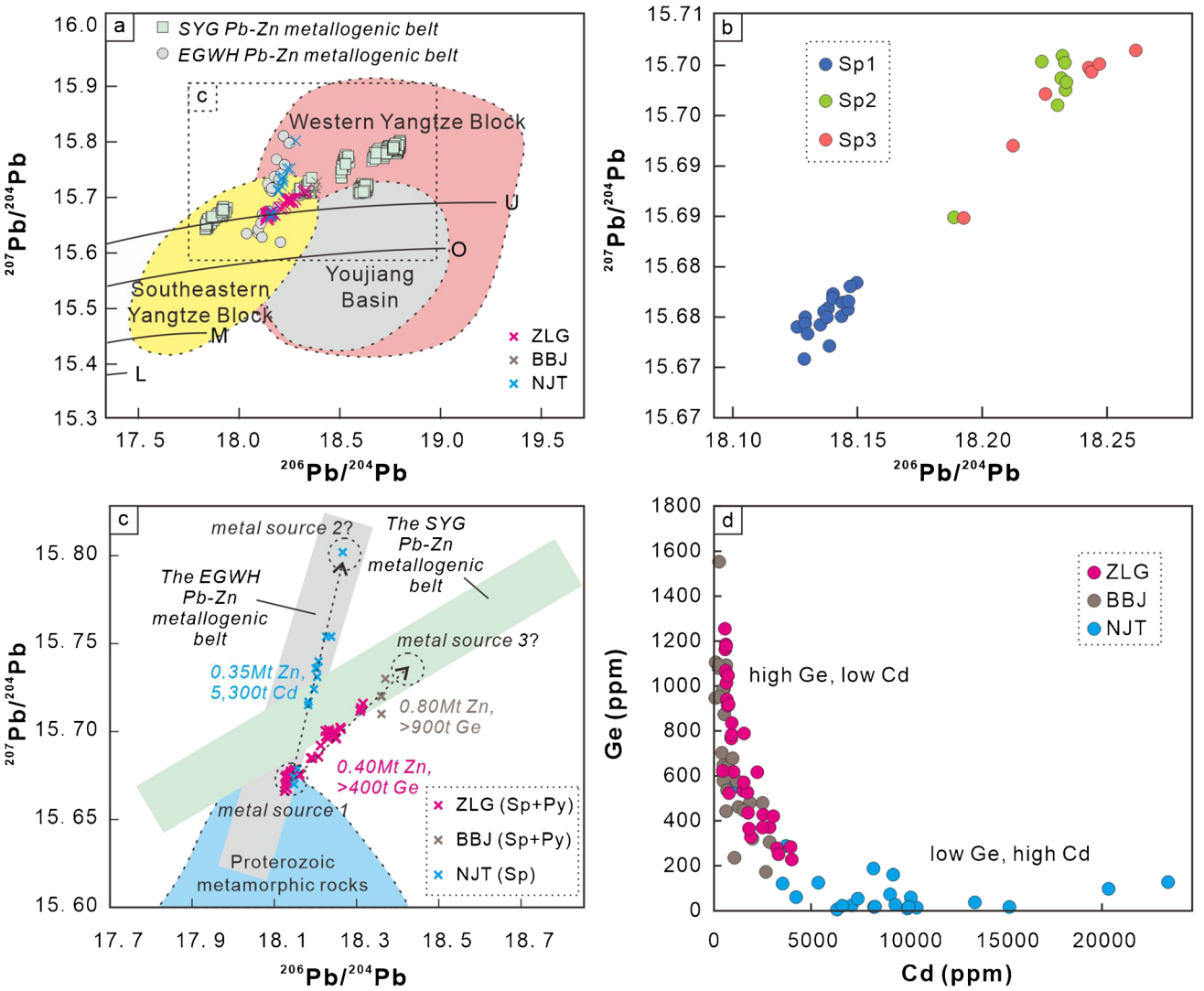

Fig. 11 (a) Comparison plot of Pb isotope ratios $^{207}Pb/^{204}Pb$ vs. $^{206}Pb/^{204}Pb$ among the Zhulingou (ZLG), Banbianjie (BBJ), Niujiaotang (NJT), other deposits from the SYG and EGWH carbonate-hosted Pb–Zn metallogenic belts, basement rocks in the western and southeastern margins of the Yangtze Block, and low-temperature hydrothermal deposits from the Youjiang basin on the southern margin of the Yangtze Block (data from Hu et al. 2015a, b). The data of the Niujiaotang and Banbianjie are from Ye et al. (2011, 2012) and Sun unpublished data, respectively. Data for Upper Continental Crust (U), Orogen Belt (O), Mantle (M), and Lower Continental Crust (L) are from Zartman and Doe (1981). (b) Comparison plot of Pb isotope ratios $^{207}Pb/^{204}Pb$ vs. $^{206}Pb/^{204}Pb$ between Sp1, Sp2, and Sp3. Sp1 and Sp2-Sp3 are discriminated. (c) Comparison plot of Pb isotope ratios $^{207}Pb/^{204}Pb$ vs. $^{206}Pb/^{204}Pb$ of sulfides among the Zhulingou, Banbianjie, and Niujiaotang carbonate-hosted Pb–Zn deposits in the EGWH (gray box) and SYG (light green box) metallogenic belts (data from Ye et al. 2012; Cai et al. 2014; Zhou et al. 2016; Luo et al. 2020). (d) Binary plots of Ge vs. Cd of sphalerite from the Zhulingou and Banbianjie Ge-rich, and Niujiaotang Cd-rich deposits

mixed type between stages I and II related to the overgrowth of euhedral Sp3 in acicular Sp1.

Implications on substitution mechanisms

Sphalerite is assumed to incorporate several minor and trace elements (Mn, Fe, Ge, Cd, etc.) in its crystallographic structure (Cook et al. 2009). Germanium is commonly positively correlated to monovalent cations such as Cu^+ or Ag^+, which suggests coupled substitution with Zn (Cook et al. 2009; Belissont et al. 2014; Cugerone et al. 2021). Nonetheless, in Cu- or Ag-depleted sphalerite, Ge may also be concentrated in the sphalerite lattice (Cook et al. 2015; Hu et al. 2021) which suggests the presence of other substitution mechanisms such as direct substitution of Ge with Zn (with a vacancy; Cook et al. 2015) or coupled substitution with divalent cations (Yuan et al. 2018).

At Zhulingou, there is no positive correlation with poorly concentrated monovalent cations (i.e., Cu, Ag) (Fig. 12),

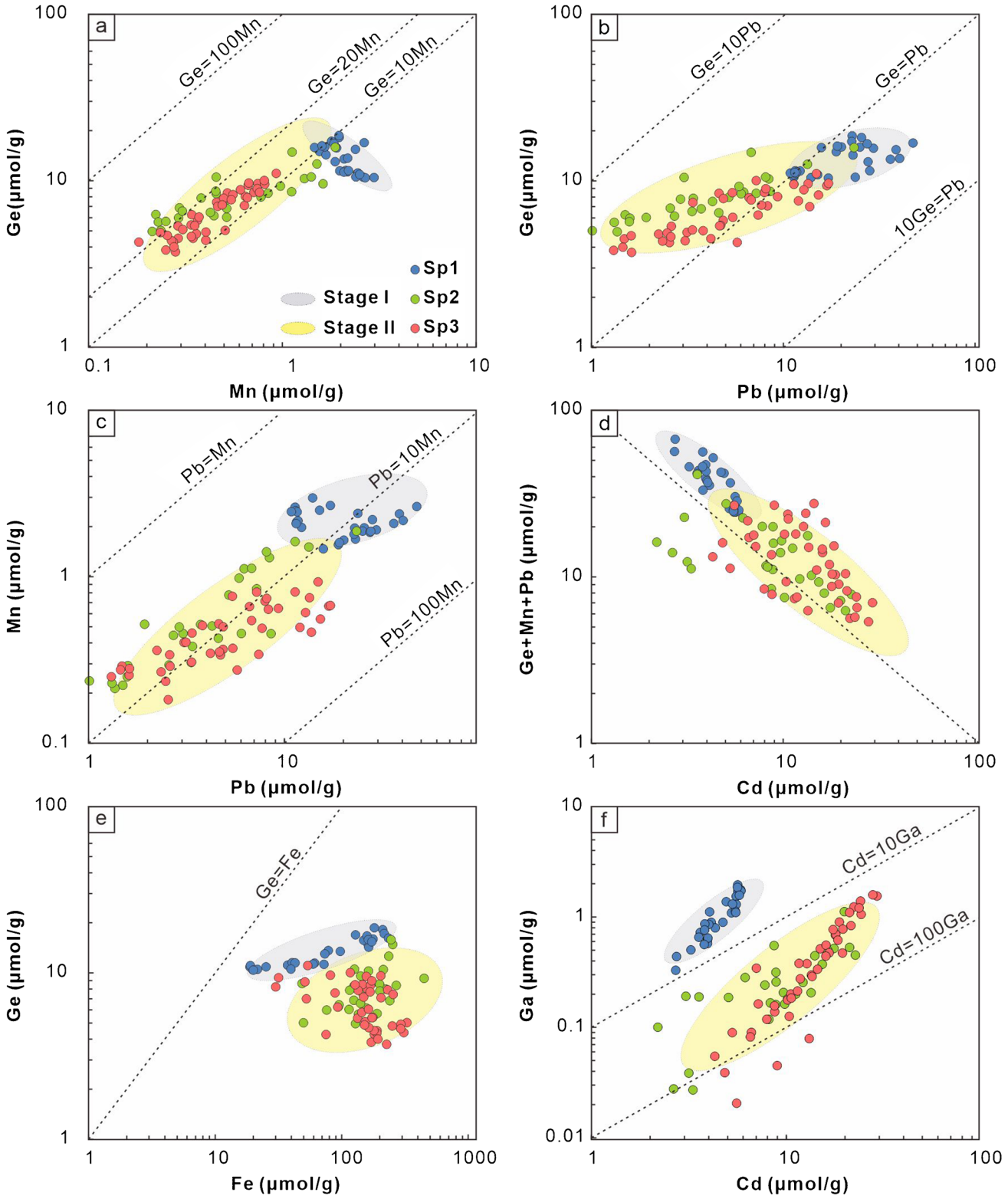

Fig. 12 Binary plots of Ge vs. Mn (a); Ge vs. Pb (b); Mn vs. Pb (c); Ge + Mn + Pb vs. Cd (d); Ge vs. Fe (e); and Ga vs. Cd (f); of the three types of sphalerite from the Zhulingou carbonate-hosted Zn(-Ge) deposit

similar to Cook et al. (2015). Numerous positive or negative correlations are reported between Ge and several cations which are commonly known as divalent in the sphalerite system (Mn^{2+}, Pb^{2+}, and Cd^{2+}; Fig. 12). This is consistent with high SSIM values among Ge, Mn, Cd, and Pb (ESM 1) that imply their high affinity. Therefore, a positive correlation between Ge and Pb + Mn molar concentrations is identified (Fig. 12a–c) as well as a negative correlation between Ge + Pb + Mn and Cd molar concentrations (Fig. 12d). No X-ray absorption near edge structure spectroscopy (XANES) study is yet available for this type of Ge(-Pb-Mn-Cd) rich sphalerite. Considering the two oxidation states of Ge (Ge^{2+} and Ge^{4+}), we suggest two possible substitution mechanisms for the incorporation of Ge into the sphalerite lattice:

$$Ge^{4+} + M^{2+} + \text{vacancy} \leftrightarrow 3(Zn, Cd)^{2+} \quad (1)$$

$$Ge^{2+} + M^{2+} \leftrightarrow 2(Zn, Cd)^{2+} \quad (2)$$

where M = Pb, (Mn). Evidence of coupled correlations between Ge and Pb or Ge and Mn is poorly documented in the literature, but their chemical behavior is similar under specific conditions (ESM 3). For example, the Ge-Pb substitution is reported in few minerals under probable oxidizing conditions such as anglesite and cerussite (Tsumeb mine; Frondel and Ito 1957) or in galena (Ambrosia-Fagundes Brazilian carbonate-hosted deposits; Monteiro et al. 2006). In these examples, especially in anglesite and cerussite, Ge is believed to be incorporated in a divalent state but no XANES study is available. Similarly, in the sphalerite from Zhulingou, XANES analyses are needed to identify the oxidation state of Ge.

No consistent correlation between Fe and Ge is observed in our data which precludes a direct control of Fe concentration on Ge incorporation (Cook et al. 2015; Fig. 12e). In the three sphalerite types, Ga and Cd are positively correlated (Fig. 12f) and in Sp1, Ga-Cd ratio (0.12–0.34) is higher than in Sp2–Sp3 (< 0.06). Such variations in the Ga-Cd ratios may indicate differences in primary fluid compositions and/or conditions of sphalerite formation (such as crystal growth rate and pH).

The formation and chemistry of acicular and euhedral sphalerite

The acicular sphalerite texture is difficult to observe under the microscope and can be confused with common euhedral sphalerite, especially in dark specimens under transmitted light (Pring et al. 2020). At Zhulingou, acicular sphalerite is the main Ge-bearing phase, with 770–1381 and 367–1174 ppm Ge in Sp1 and Sp2, respectively. Nonetheless, in Sp2, euhedral grains similar to Sp3 following concentric colloform bands appear systematically with light-yellow color and are largely depleted in metals (e.g., Ge, Ga) compared to co-existing acicular grains with high Ge concentrations, especially those close to the boundary between acicular and coarse-euhedral (Fig. 8).

Sulfur isotope and trace element concentrations record critical information on the formation of various types of sphalerite (Kelley et al. 2004; Cook et al. 2009). Considering the absence of sulfates at Zhulingou, $\delta^{34}S$ values of sulfides could represent the total sulfur isotopic composition ($\delta^{34}\sum S$) of the fluid from which the sulfides precipitated and thus can be used to directly trace the sulfur sources (Ohmoto 1972). All sphalerite samples have negative $\delta^{34}S$ values from −14.6 to −6.8‰, which are significantly lower than that of Devonian seawater ($\delta^{34}S_{seawater}$ = +17‰ to +34‰; Claypool et al. 1980). Because thermochemical sulfate reduction ($\Delta^{34}S$ = 15–20‰; Machel et al. 1995) is unable to achieve such a high level of fractionation of sulfur isotopes, a plausible explanation for the low $\delta^{34}S$ values of sulfides at Zhulingou is the formation of S^{2-} by bacterial sulfate reduction (BSR) ($\Delta^{34}S$ = 40–60‰; Machel 2001; Basuki et al. 2008) of Devonian sulfate. Furthermore, BSR occurred in sulfate-open to relatively sulfate-closed systems (Ohmoto and Rye 1979), causing slightly lighter sulfur isotopes of acicular colloform sphalerite ($\delta^{34}S$ = −14.6 to −9.6‰) than coarse euhedral sphalerite ($\delta^{34}S$ = −9.2 to −6.8‰).

Three hypotheses are proposed to explain the chemical conditions leading to acicular sphalerite with higher Ge enrichment: (i) low temperature (Bernstein 1985; Frenzel et al. 2016; Bauer et al. 2019), high sulfur fugacity (fS_2) (Kelley et al. 2004; Bonnet et al. 2017), and low pH (Pattrick et al. 1993), which may increase Ge solubility in the fluid; (ii) mineral precipitation rate and related acicular grain formation may be a consequence of local variations in temperature, pressure and/or supersaturation state (Roedder 1968; Beaudoin 2000; Liu et al. 2015; Song et al. 2020). During successive mineralizing pulses or cycles, fast mineral growth rate could form acicular grains and uptake a large amount of trace metals including Ge from the fluid, whereas the last remaining metal concentrations in fluid precipitate in euhedral grains which have grown slowly (Lorens 1981; Barker and Cox 2011); (iii) crystallographic characteristics of the acicular texture favored larger Ge incorporation into sphalerite comparatively to the euhedral texture.

Pattrick et al. (1993) reported the large influence of pH variations in Cd, Fe, Cu, and In concentrations in fluids, based on hydrolysis experimental works (no data for Ge). Hydrogen ion concentration below the first hydrolysis constant (2 or 3 log units) may enhance the adsorption of Cd in the sphalerite lattice (Jean and Bancroft 1986). Differential pH conditions of the fluid could explain variations in Ga/Cd ratios observed between Sp1 and Sp2-Sp3. Moreover, marcasite is frequently observed coexisting with acicular Ge-rich Sp1-Sp2 at Zhulingou and absent in euhedral Ge-poor Sp3. The occurrence of marcasite is frequently interpreted as

evidence of acidic fluid conditions (pH < 4–5; Murowchick and Barnes 1986; Kitchaev and Ceder 2016) and we suggest that acidic fluids may be a favorable condition for the incorporation of Ge into acicular sphalerite. In addition, a high mineral precipitation rate, assumed to be a key component in the acicular grain formation, could also be essential for the incorporation of high trace metal concentrations in sphalerite (Roedder 1968; Beaudoin 2000; Barker and Cox 2011).

Using the mineral geothermometer GGIMFis proposed by Frenzel et al. (2016), slight increase in temperature is observed between Stage I and II with 72–122 °C in Sp1 and 100–142 °C in Sp2-Sp3 (ESM 1). Bernstein (1985) proposed that high sulfur activity (fS_2) is a favorable condition to incorporate Ge in sphalerite. However, average fS_2, based on GGIMFis temperatures and Fe contents in sphalerite (Frenzel et al. 2021; ESM 1) reveal similar sulfur fugacities for the two mineralized stages, i.e., dfS_2 in Sp1 and Sp2-Sp3 are −0.31 ~ +0.33 and −0.15 ~ +0.36, respectively. Furthermore, no evidence of widespread wurtzite was found with XRD data in acicular textures (ESM 3).

Accordingly, the transition between acicular and euhedral sphalerite is likely caused by changes in precipitation conditions, including the increase in temperature and pH and decrease in oversaturation and precipitation rate (Roedder 1968; Beaudoin 2000; Pfaff et al. 2011). The acicular sphalerite (stage I) was likely formed by a high degree of

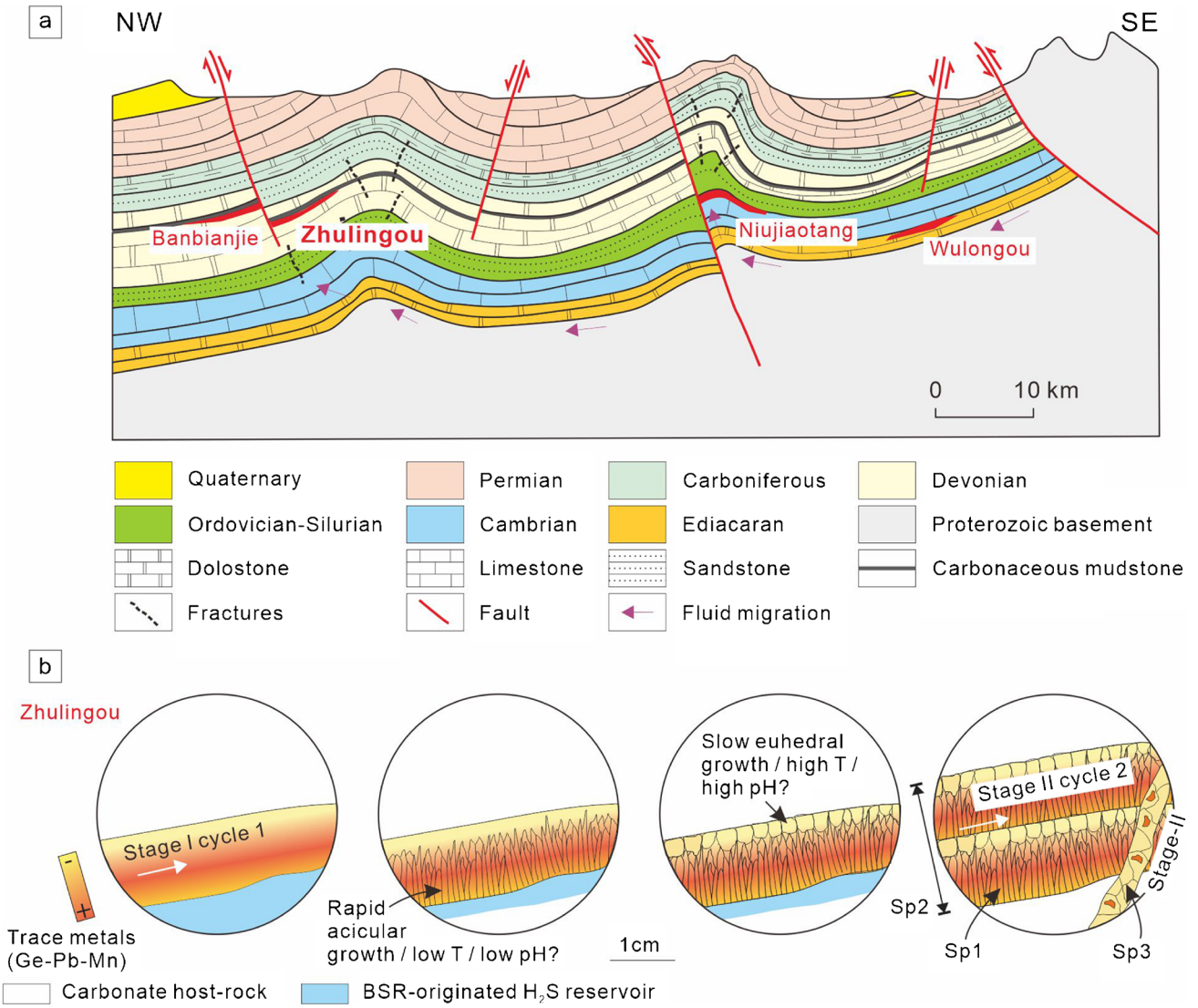

Fig. 13 (a) Simplified geodynamic model of the southwestern EGWH Pb–Zn metallogenic belt, showing migration of brine enriched in Cd or Ge and precipitating at the interface of different lithologies, commonly close to faults. (b) Sketches representing the evolution of sphalerite textures at Zhulingou. The deep hydrothermal metalliferous fluids mixed with shallow, bacteriogenic brines, which precipitated acicular colloform sphalerite, followed by euhedral sphalerite grains. Rapid growth rate, low T, and low pH allowed the precipitation of acicular textures with higher Ge, Pb, and Mn concentrations compared to euhedral sphalerite

supercooling, oversaturation, and rapid mixing between bacteriogenic sulfur and metals in open spaces, supported by dissolution collapse breccia fragments (Fig. 4a, e, f; Gagnevin et al. 2014). This process is different from the formation of the coarse euhedral sphalerite (stage II), which implies a relatively slow oversaturation and limited space. In acicular sphalerite, Ge and Pb can reach high concentrations under disequilibrium conditions due to sudden oversaturation (Pfaff et al. 2011).

In other Chinese carbonate-hosted Pb–Zn deposits, the occurrence of acicular sphalerite is suspected especially in the Lehong (Wei et al. 2019), Banbianjie, Huodehong, and Wusihe Ge-rich deposits (ESM 3). At Lehong, sphalerite with thin lamellae texture coexisting with galena probably shares a similar acicular texture with Zhulingou and shows a positive correlation between Ge and divalent cations (e.g., Fe; Wei et al. 2019). In the Huodehong deposit (Hu et al. 2021), very similar sphalerite chemistry is found, with Ge correlated to divalent cations such as Mn and Cd, but no detailed microscopic investigation is provided to document acicular textures.

A proposed genetic model of the Zhulingou Zn(-Ge) deposit.

The source and migration of Zn(-Ge)-rich fluids certainly played a key role in the regional Ge enrichment of the Zhulingou deposit. At a regional scale, the distribution of Ge-rich deposits is probably affected by the background values of Ge in sedimentary basins (Bonnet et al. 2014; Du et al. 2019). On the margins of the Yangtze Block, Ge concentrations in the Proterozoic basement (0.96–1.80 ppm) are higher than in the sedimentary sandstone and carbonate rocks (0.05–1.34 ppm) (Du et al. 2019). Although Ge may be significantly enriched in surrounding carbonaceous sediments (Fig. 5b), the amount of carbonaceous mudstone layers is relatively low at the regional scale and generally, in the Banbianjie-Zhulingou district (An et al. 2022). Lead isotopic data of carbonate-hosted Pb–Zn deposits in South China plot close to the metamorphic basement rocks field (Fig. 11a), suggesting that the metals were derived from the Proterozoic basement (Luo et al. 2019).

A regional comparison of Pb isotopic data shows significant differences in trends between the two main carbonate-hosted Pb–Zn metallogenic districts in South China (Cd-rich EGWH and Ge-rich SYG; Fig. 11c). Our data in the Banbianjie-Zhulingou district follow the SYG trend and not EGWH Pb isotope trend, which implies different origins between the Ge-rich Banbianjie-Zhulingou and Cd-rich Nuijiaotang Pb–Zn districts. Such variations in Pb isotope may be related to the mixing of a common metal source 1 with two different metal sources 2 and 3, enriched in Cd and Ge, respectively (Fig. 11c). Another possibility is the presence of one single fluid, which evolved during migration in the sedimentary basin, implying selective changes in Pb isotope and Cd-Ge concentrations (Gigon et al. 2020). The second hypothesis is more likely especially if we consider the negative correlation between Ge and Cd, with a general high Cd/Ge ratio at Niujiaotang and low Cd/Ge ratio at the Banbianjie-Zhulingou district (Fig. 11d). Differences in Cd concentrations may indicate various fluid- and mineralization types, as previously suggested by Cugerone et al (2021). Hence, at regional/district scales, the Cd enrichment may be an indirect key parameter to identify Ge enrichment in the deposit.

Hence, a genetic model is proposed to explain Ge-rich carbonate-hosted mineralization in the Zhulingou deposit in relationship with nearby deposits (e.g. Banbianjie and Niujiaotang; Fig. 13a). In the southeastern margin of the Yangtze Block, low-temperature basinal brines migrated from the west side of the Jiangnan orogenic foreland, along unconformities where Ge and Cd were likely scavenged from local Ge and Cd-rich sedimentary or metamorphic rocks. Fluid differentiation led to the formation of Cd and Ge-rich deposits. At Zhulingou, the Ge-rich fluids may have been driven by upward flow along the regional Huangsi fault system and trapped into the evaporitic dolostone and organic-rich carbonaceous mudstone of the Devonian Wangchengpo Formation. Mixing between shallow, bacteriogenic brines and deep hydrothermal metalliferous fluids formed dissolution collapse breccia and precipitate acicular colloform sphalerite in open spaces, followed by euhedral sphalerite grains (Fig. 13b). Low T, pH, high oversaturation, and growth rate seem to be key factors enhancing the precipitation of acicular textures and the incorporation of Ge in sphalerite.

Conclusion

1) Two mineralization stages are recognized in the Zhulingou carbonate-hosted Zn(-Ge) deposit. The primary mineralizing fluid (stage I) formed type 1 strata-bound breccia ore, composed of acicular sphalerite (Sp1) and with high Ge concentrations (up to ~ 1000 ppm Ge). Following a gradual chemical evolution, a secondary hydrothermal fluid (stage II, slightly post–stage I) led to the formation of type 3 stockwork euhedral sphalerite (Sp3), with lower Ge concentrations (up to ~ 500 ppm). Type 1 ore mixed with local presence of Sp3, formed acicular-euhedral sphalerite (Sp2).
2) Ge incorporation in sphalerite is mostly coupled to divalent cations such as Pb, Mn and Cd in absence of significative concentrations of Cu and Ag monovalent cations. Two substitution mechanisms are proposed, depending on the two possible Ge oxidation

states: $Ge^{4+} + M^{2+} + \text{vacancy} \leftrightarrow 3(Zn,Cd)^{2+}$ and/or $Ge^{2+} + M^{2+} \leftrightarrow 2(Zn, Cd)^{2+}$ with M = Pb, (Mn).

3) Fluid mixing of basement-derived, and Ge-rich metalliferous fluids with a reservoir of BSR sulfur probably leads to rapid oversaturation of the fluids under low-temperature (< 150 °C). Such process formed acicular sphalerite with higher Ge content than in coarse-euhedral sphalerite. This study shows the importance of combining textural and chemical observations in carbonate-hosted deposits to target Ge concentrations.

Supplementary Information The online version contains supplementary material available at https://doi.org/10.1007/s00126-022-01112-4.

Acknowledgements We thank De-Zhi Yang and Xiu-Wen Luo for the help in fieldwork, Nigel J. Cook (University of Adelaide, Australia), and Denis Fougerouse (Curtin University, Australia) for fruitful discussions. Comments and suggestions from Georges Beaudoin (Editor-in-chief), Shao-Yong Jiang (Associate Editor), and three anonymous reviewers greatly improved the quality of the paper.

Funding This research was financially supported by the fund from the National Natural Science Foundation of China (42172082; 41872095 and U1812402) and the Talents Program Project of Yunnan Province (YNQR-QNRC-2018–104).

Declarations

Competing interests The authors declare no competing interests.

References

An YL, Luo K, Zhou JX, Nguyen A, Lu MD, Meng QT, An Q (2022) Origin of the Devonian carbonate-hosted Banbianjie Ge-Zn deposit, Guizhou Province, South China: geological, mineralogical and geochemical constraints. Ore Geol Rev 142:104696

Anderson GM (1975) Precipitation of Mississippi Valley-type ores. Econo Geol 70:937–942

Barker SL, Cox SF (2011) Oscillatory zoning and trace element incorporation in hydrothermal minerals: insights from calcite growth experiments. Geofluids 11:48–56

Basuki NI, Taylor BE, Spooner ETC (2008) Sulfur isotope evidence for thermochemical reduction of dissolved sulfate in Mississippi Valley-type zinc-lead mineralization, Bongara Area, Northern Peru. Econo Geol 103:783–799

Bauer ME, Burisch M, Ostendorf J, Krause J, Frenzel M, Seifert T, Gutzmer J (2019) Trace element geochemistry of sphalerite in contrasting hydrothermal fluid systems of the Freiberg district, Germany: insights from LA-ICP-MS analysis, near-infrared light microthermometry of sphalerite-hosted fluid inclusions, and sulfur isotope geochemistry. Mineral Deposita 54:237–262

Beaudoin G (2000) Acicular sphalerite enriched in Ag, Sb, and Cu embedded within color-banded sphalerite from the Kokanee Range, British Columbia, Canada. Can Mineral 38:1387–1398

Belissont R, Boiron MC, Luais B, Cathelineau M (2014) LA-ICP-MS analyses of minor and trace elements and bulk Ge isotopes in zoned Ge-rich sphalerites from the Noailhac - Saint-Salvy deposit (France): insights into incorporation mechanisms and ore deposition processes. Geochim Cosmochim Ac 126:518–540

Bernstein LR (1985) Germanium geochemistry and mineralogy. Geochim Cosmochim Ac 49:2409–2422

Bonnet J, Mosser-Ruck R, André-Mayer AS, Cauzid J, Bailly L (2014) Germanium distribution in Sphalerite from North-East America MVT Deposits: a Multiscale Study. Acta Geol Sin-Eng Ed 2:437–439

Bonnet J, Cauzid J, Testemale D, Kieffer I, Proux O, Lecomte A, Bailly L (2017) Characterization of germanium speciation in sphalerite (ZnS) from Central and Eastern Tennessee, USA, by x-ray absorption spectroscopy. Minerals 7:79

Cai YX, Yang HM, Duan RC, Lu SZ, Zhang LG, Liu CP, Qiu XF (2014) Fluid inclusions and S, Pb, C isotope geochemistry of Pb-Zn deposits hosted by Lower Cambrian in Western Hunan-Eastern Guizhou area. Geoscience 28:29–41 ((**in Chinese with English abstract**))

Carter A, Roques D, Bristow C, Kinny P (2001) Understanding Mesozoic accretion in Southeast Asia: significance of Triassic thermotectonism (Indosinian orogeny) in Vietnam. Geology 29:211–214

Claypool GE, Holser WT, Kaplan IR, Sakai H, Zak I (1980) The age curves of sulfur and oxygen isotopes in marine sulfate and their mutual interpretation. Chem Geol 28:199–260

Cook NJ, Ciobanu CL, Pring A, Skinner W, Shimizu M, Danyushevsky L, Saini-Eidukat B, Melcher F (2009) Trace and minor elements in sphalerite: a LA-ICPMS study. Geochim Cosmochim Ac 73:4761–4791

Cook NJ, Etschmann B, Ciobanu CL, Geraki K, Howard DL, Williams T, Rae N, Pring A, Chen G, Johannessen B (2015) Distribution and substitution mechanism of Ge in a Ge-(Fe)-bearing sphalerite. Minerals 5:117–132

Craddock PR, Rouxel OJ, Ball LA, Bach W (2008) Sulfur isotope measurement of sulfate and sulfide by high-resolution MC-ICP-MS. Chemi Geol 253:102–113

Cugerone A, Cenki-Tok B, Chauvet A, Le Goff E, Bailly L, Alard O, Allard M (2018) Relationships between the occurrence of accessory Ge-minerals and sphalerite in Variscan Pb-Zn deposits of the Bossost anticlinorium, French Pyrenean Axial Zone: Chemistry, microstructures and ore-deposit setting. Ore Geol Rev 95:1–19

Cugerone A, Cenki-Tok B, Munoz M, Kouzmanov K, Oliot E, Motto-Ros V, Le GE (2021) Behavior of critical metals in metamorphosed Pb-Zn ore deposits: example from the Pyrenean Axial Zone. Mineral Dep 56:685–705

Dai CG, Hu MY, Chen JS, Wang M, Wang XH (2015) The important geologic events of Guizhou province and its geologic significance. Guizhou Geology 32:1–14 ((**in Chinese with English abstract**))

Du SJ, Wen HJ, Zhu CW, Luo CG, Zhou ZB, Yang ZM, Chen JS, Zhu X (2019) Geochemical background on the super-richening of disperse metal elements on the western margin of the Yangtze plate. Acta Petrol Sin 35:3355–3369 ((**in Chinese with English abstract**))

Etschmann B, Liu WH, Li K, Dai S, Reith F, Falconer D, Kerr G, Paterson D, Howard D, Kappen P, Wykes J, Brugger J (2017) Enrichment of germanium and associated arsenic and tungsten in coal and roll-front uranium deposits. Chem Geol 463:29–49

European Commission (2020) Study on the EU's list of Critical Raw Materials Critical Raw Materials, Factsheets (Final). Directorate-General for Internal Market, Industry, Entrepreneurship and SMEs, Joint Research Centre Directorate GROW.C, JRC.D Unit GROW.C.2 Energy-intensive Industries and Raw Materials, JRC.D.3 Land Resources, pp 1–819

Feng Y, Zhang W, Hu Z, Liu Y, Chen K, Fu JL, Xie JY, Shi QH (2018) Development of sulfide reference materials for in situ platinum group elements and S-Pb isotope analyses by LA-(MC)-ICP-MS. J Anal Atom Spectrom 33:2172–2183

Frenzel M, Ketris MP, Gutzmer J (2014) On the geological availability of germanium. Mineral Deposita 49:471–486

Frenzel M, Hirsch T, Gutzmer J (2016) Gallium, germanium, indium, and other trace and minor elements in sphalerite as a function of deposit type - a meta-analysis. Ore Geol Rev 76:52–78

Frenzel M, Voudouris P, Cook NJ, Ciobanu CL, Gilbert S, Wade BP (2021) Evolution of a hydrothermal ore-forming system recorded by sulfide mineral chemistry: a case study from the Plaka Pb-Zn-Ag Deposit, Lavrion, Greece. Mineral Deposita 57:417–438

Frondel C, Ito J (1957) Geochemistry of germanium in the oxidized zone of the Tsumeb mine, South-West Africa. Am Mineral 42:743–753

Fu JL, Hu ZC, Zhang W, Yang L, Liu YS, Li M, Zong KQ, Gao S, Hu SH (2016) In situ sulfur isotopes ($\delta^{34}S$ and $\delta^{33}S$) analyses in sulfides and elemental sulfur using high sensitivity cones combined with the addition of Nitrogen by laser ablation MC-ICP-MS. Anal Chim Acta 911:14–26

Gagnevin D, Menuge JF, Kronz A, Barrie C, Boyce AJ (2014) Minor elements in layered sphalerite as a record of fluid origin, mixing, and crystallization in the Navan Zn-Pb ore deposit, Ireland. Econo Geol 109:1513–1528

Gao S, Yang J, Zhou L, Li M, Hu ZC, Guo JL, Yuan HL, Gong HJ, Xiao GQ, Wei JQ (2011) Age and growth of the Archean Kongling Terrain, South China, with emphasis on 3.3 Ga granitoid gneisses. Am J Sci 311:153–182

Gigon J, Deloule E, Mercadier J, Huston DL, Richard A, Annesley IR, Wygralak AS, Skirrow RG, Mernagh TP, Masterman K (2020) Tracing metal sources for the giant McArthur River Zn-Pb deposit (Australia) using lead isotopes. Geology 48:478–482

Gunn (2014) Critical Metals Handbook. Wiley, New York

Höll R, Kling M, Schroll E (2007) Metallogenesis of germanium-a review. Ore Geol Rev 30:145–180

Hu RZ, Mao JW, Hua RM, Fan WM (2015a) Intracontinental mineralization in the South China Block. Science Press, Beijing (**(in Chinese)**)

Hu ZC, Zhang W, Liu YS, Gao S, Li M, Zong KQ, Chen HH, Hu SH (2015b) "Wave" signal-smoothing and mercury-removing device for laser ablation quadrupole and multiple collector ICPMS analysis: application to lead isotope analysis. Anal Chem 87:1152–1157

Hu RZ, Fu SL, Huang Y, Zhou MF, Fu SH, Zhao CH, Wang YJ, Bi XW, Xiao JF (2017) The giant South China Mesozoic low-temperature metallogenic domain: reviews and a new geodynamic model. J Asian Earth Sci 137:9–34

Hu YS, Wei C, Ye L, Huang ZL, Danyushevsky L, Wang HY (2021) LA-ICP-MS sphalerite and galena trace element chemistry and mineralization-style fingerprinting for carbonate-hosted Pb-Zn deposits: perspective from Early Devonian Huodehong deposit in Yunnan, South China. Ore Geol Rev 136:104253

Jean GE, Bancroft GM (1986) Heavy metal adsorption by sulphide mineral surfaces. Geochim Cosmochim Ac 50:1455–1463

Ji XJ (2019) Occurrence of germanium and element alternative mechanism in sphalerite from Huize Pb-Zn deposit. Master's thesis. University of Chinese Geosciences (Beijing) (in Chinese with English Abstract)

Johan Z (1988) Indium and germanium in the structure of sphalerite - an example of coupled substitution with copper. Miner Petrol 39:211–229

Kelley KD, Leach DL, Johnson CA, Clark JL, Fayek M, Slack JF, Anderson VM, Ayuso RA, Ridley WI (2004) Textural, compositional, and sulfur isotope variations of sulfide minerals in the Red Dog Zn-Pb-Ag deposits, Brooks Range, Alaska: Implications for Ore Formation. Econo Geol 99:1509–1532

Kitchaev DA, Ceder G (2016) Evaluating structure selection in the hydrothermal growth of FeS_2 pyrite and marcasite. Nat Commun 7:1–7

Leach DL, Song YC (2019) Sediment-hosted zinc-lead and copper deposits in China: Society of Economic Geologists. Special Publication 22:325–409

Licht C, Peiró LT, Villalba G (2015) Global substance flow analysis of gallium, germanium, and indium: quantification of extraction, uses, and dissipative losses within their anthropogenic cycles. J Ind Ecol 19:890–903

Liu YC, Yang ZS, Tian SH, Song YC, Zhang HR (2015) Fluid origin of fluorite-rich carbonate-hosted Pb-Zn mineralization of the Himalayan-Zagros collisional orogenic system: a case study of the Mohailaheng deposit, Tibetan Plateau, China. Ore Geol Rev 70:546–561

Lorens RB (1981) Sr, Cd, Mn and Co distribution coefficients in calcite as a function of calcite precipitation rate. Geochim Cosmochim Ac 45:553–561

Luo K, Zhou JX, Huang ZL, Wang XC, Wilde SA, Zhou W, Tian LY (2019) New insights into the origin of early Cambrian carbonate-hosted Pb-Zn deposits in South China: a case study of the Maliping Pb-Zn deposit. Gondwana Res 70:88–103

Luo K, Zhou JX, Huang ZL, Caulfield J, Zhao JX, Feng YX, Ouyang H (2020) New insights into the evolution of Mississippi Valley-Type hydrothermal system: a case study of the Wusihe Pb-Zn deposit, South China, using quartz in-situ trace elements and sulfides in situ S-Pb isotopes. Am Mineral 105:35–51

Machel HG (2001) Bacterial and thermochemical sulfate reduction in diagenetic settings - old and new insights. Sediment Geol 140:143–175

Machel HG, Krouse HR, Sassen R (1995) Products and distinguishing criteria of bacterial and thermochemical sulfate reduction. Appl Geochem 10:373–389

Mondillo N, Arfè G, Herrington R, Boni M, Wilkinson C, Mormone A (2018) Germanium enrichment in supergene settings: evidence from the Cristal nonsulfide Zn prospect, Bongará district, northern Peru. Mineral Deposita 53:155–169

Monteiro SLV, Bettencourt SJ, Juliani C, de Oliveira TF (2006) Geology, petrography, and mineral chemistry of the Vazante non-sulfide and Ambrosia and Fagundes sulfide-rich carbonate-hosted Zn-(Pb) deposits, Minas Gerais, Brazil. Ore Geol Rev 28:201–234

Murowchick JB, Barnes HL (1986) Marcasite precipitation from hydrothermal solutions. Geochim Cosmochim Ac 50:2615–2629

Nakai SI, Halliday AN, Kesler SE, Jones HD, Kyle JR, Lane TE (1993) Rb-Sr dating of sphalerites from Mississippi Valley-type (MVT) ore deposits. Geochim Cosmochim Ac 57:417–427

Ohmoto H (1972) Systematics of sulfur and carbon isotopes in hydrothermal ore deposits. Econo Geol 67:551–578

Ohmoto H, Rye RO (1979) Isotopes of sulfur and carbon. In: Barnes HL (ed) Geochemistry of hydrothermal ore deposits, 2nd edn. Wiley-Interscience, New York, pp 509–567

Paton C, Woodhead JD, Hellstrom JC, Hergt JM, Greig A, Maas R (2010) Improved laser ablation U-Pb zircon geochronology through robust downhole fractionation correction. Geochem Geophy Geosy 11:1–36

Pattrick RA, Dorling M, Polya DA (1993) TEM study of indium-bearing and copper-bearing growth-banded sphalerite. Can Mineral 31:105–117

Pearce NJ, Perkins WT, Westgate JA, Gorton MP, Jackson SE, Neal CR, Chenery SP (1997) A compilation of new and published major and trace element data for NIST SRM 610 and NIST SRM 612 glass reference materials. Geostandard Newslett 21:115–144

Pedder A (1972) Species of the tetracoral genus temnophyllum from givetian/frasnian boundary beds of the district of Mackenzie, Canada. J Paleontol 46:696–710

Pfaff K, Koenig A, Wenzel T, Ridley I, Hildebrandt LH, Leach DL, Markl G (2011) Trace and minor element variations and sulfur isotopes in crystalline and colloform ZnS: incorporation mechanisms and implications for their genesis. Chem Geol 286:118–134

Pring A, Wade B, McFadden A, Lenehan CE, Cook NJ (2020) Coupled substitutions of minor and trace elements in co-existing sphalerite and wurtzite. Minerals 10(2):147

Qiu L, Yan DP, Tang SL, Wang Q, Yang WX, Tang X, Wang J (2016) Mesozoic geology of southwestern China: Indosinian foreland overthrusting and subsequent deformation. J Asian Earth Sci 122:91–105

Roedder E (1968) The non-colloidal origin of 'colloform' textures in sphalerite ores. Econo Geol 63:451–471

Sahlström F, Arribas A, Dirks P, Corral I, Chang Z (2017) Mineralogical distribution of germanium, gallium and indium at the Mt Carlton high-sulfidation epithermal deposit, NE Australia, and comparison with similar deposits worldwide. Minerals 7:213

Schulz KJ, DeYoung JHJ, Seal II RR, Bradley DC (2017) Critical mineral resources of the United States - economic and environmental geology and prospects for future:U.S. geological survey professional paper 1802. U.S. Geological Survey

Smith KS, Huyck HLO (1999) An overview of the abundance, relative mobility, bioavailability, and human toxicity of metals. The Environmental Geochemistry of Mineral Deposits 6:29–70

Song YC, Hou ZQ, Xue CD, Huang SQ (2020) New mapping of the world-class Jinding Zn-Pb deposit, Lanping basin, southwest China: genesis of ore host rocks and records of hydrocarbon-rock interaction. Econo Geol 115:981–1002

Tao Y, Hu RZ, Tang YY, Ye L, Qi HW, Fan HF (2019) Types of dispersed elements bearing ore-deposits and their enrichment regularity in Southwest China. Acta Geol Sin 93:1210–1230 (**(in Chinese with English abstract)**)

Wang Z, Bovik AC, Sheikh HR, Simoncelli EP (2004) Image quality assessment: from error visibility to structural similarity. IEEE T Image Process 13:600–612

Wei C, Ye L, Hu YS, Danyushevskiy L, Li ZL, Huang ZL (2019) Distribution and occurrence of Ge and related trace elements in sphalerite from the Lehong carbonate-hosted Zn-Pb deposit, northeastern Yunnan, China: Insights from SEM and LA-ICP-MS studies. Ore Geol Rev 115:103175

Wen HJ, Zhou ZB, Zhu CW, Luo CG, Wang DZ, Du SJ, Li XF, Chen MH, Li HY (2019) Critical scientific issues of super-enrichment of dispersed metals. Acta Petrol Sin 35:3271–3291 (**(in Chinese with English abstract)**)

Wilson SA, Ridley WI, Koenig AE (2002) Development of sulfide calibration standards for the laser ablation inductively-coupled plasma mass spectrometry technique. J Anal Atom Spectrom 17:406–409

Wu Y, Kong ZG, Chen MH, Zhang CQ, Cao L, Tang YJ, Yuan X, Zhang P (2019) Trace elements in sphalerites from the Mississippi Valley-type lead-zinc deposits around the margins of Yangtze Block and its geological implications: A LA-ICPMS study. Acta Petrol Sin 35:3443–3460 (**(in Chinese with English abstract)**)

Wu T, Huang ZL, Ye L, Wei C, Chen J, Yang M, Yan ZF, Sui Z (2021) Origin of the carbonate-hosted Danaopo Zn-Pb deposit in western Hunan Province, China: geology and in-situ mineral S-Pb isotope constraints. Ore Geol Rev 129:103941

Wu T, Wang XC, Wilde SA, Li QL, Pang CJ, Zhou JX (2022) Decoupling of isotopes between magmatic zircons and their mafic host rocks: a case study from the ca. 830 Ma Jiabang dolerite. South China. Precambrian Res 369:106519

Yan DP, Zhou MF, Song HL, Wang XW, Malpas J (2003) Origin and tectonic significance of a Mesozoic multi-layer over-thrust system within the Yangtze Block (South China). Tectonophysics 361:239–254

Yang DZ, Zhou JX, Luo K, Yu J, Zhou ZH (2020) New discovery of Zhulingou zinc deposit in Guiding County, Guizhou and its research value. Bulletin of Mineralogy, Petrology and Geochemistry 39:344–345 (**(in Chinese)**)

Yang ZM, Zhou JX, Luo K, Yang DZ, Yu J, Zhou FC (2021a) Mineralogy and mineral chemistry of carbonates from the Zhulingou Ge-Zn deposit in Guizhou Province and its geological significance. Acta Petrol Sin 37:2743–2760 (**(in Chinese with English abstract)**)

Yang Q, Zhang XJ, Ulrich T, Zhang J, Wang J (2021b) Trace element compositions of sulfides from Pb-Zn deposits in the Northeast Yunnan and Northwest Guizhou Provinces, SW China: Insights from LA-ICP-MS analyses of sphalerite and pyrite. Ore Geol Rev 141:104639

Yang SP, Yang SY, An Q (2017) Comparison of characteristics of lead-zinc deposits in South Guizhou Province. In: Abstracts of the 8th National Symposium on Metallogenic Theory and Prospecting Methods. Nanchang: Editorial Department of Acta Mineralogica Sinica p 863 (in Chinese)

Ye L, Cook NJ, Ciobanu CL, Yuping L, Qian Z, Tiegeng L, Wei G, Yulong Y, Danyushevskiy L (2011) Trace and minor elements in sphalerite from base metal deposits in South China: a LA-ICPMS study. Ore Geol Rev 39:188–217

Ye L, Cook NJ, Liu T, Ciobanu CL, Gao W, Yang Y (2012) The Niujiaotang Cd-rich zinc deposit, Duyun, Guizhou province, southwest China: ore genesis and mechanisms of cadmium concentration. Mineral Deposita 47:683–700

Yuan B, Zhang CQ, Yu HJ, Yang YM, Zhao YX, Zhu CC, Ding QF, Zhou YB, Yang JC, Xu Y (2018) Element enrichment characteristics: insights from element geochemistry of sphalerite in Daliangzi Pb-Zn deposit, Sichuan, Southwest China. J Geochem Explor 186:187–201

Zartman RE, Doe BR (1981) Plumbotectonics - the Model. Tectonophys 75:135–162

Zhang W, Hu ZC, Gunther D, Liu YS, Ling WL, Zong KQ, Chen HH, Gao S, Xu L (2016) Direct lead isotope analysis in Hg-rich sulfides by LA-MC-ICP-MS with a gas exchange device and matrix-matched calibration. Anal Chim Acta 948:9–18

Zhang JW, Ye TP, Dai YR, Chen JS, Zhang H, Dai CG, Yuan GH, Jiang KY (2019) Provenance and tectonic setting transition as recorded in the Neoproterozoic strata, western Jiangnan Orogen: Implications for South China within Rodinia. Geosci Front 10:1823–1839

Zhang W, Hu ZC, Liu YS (2020) Iso-Compass: new freeware software for isotopic data reduction of LA-MC-ICP-MS. J Anal at Spectrom 35:1087–1096

Zhao XF, Zhou MF, Li JW, Sun M, Gao JF, Sun WH, Yang JH (2010) Late Paleoproterozoic to early Mesoproterozoic Dongchuan Group in Yunnan, SW China: implications for tectonic evolution of the Yangtze Block. Precambrian Res 182:57–69

Zhao JH, Zhou MF, Yan DP, Zheng JP, Li JW (2011) Reappraisal of the ages of Neoproterozoic strata in South China: no connection with the Grenvillian orogeny. Geology 39:299–302

Zhou MF, Yan DP, Kennedy AK, Li YQ, Ding J (2002) SHRIMP U-Pb zircon geochronological and geochemical evidence for Neoproterozoic arc-magmatism along the western margin of the Yangtze Block, South China. Earth Planet Sc Lett 196:51–67

Zhou MF, Zhao XF, Chen WT, Li XC, Wang W, Yan DP, Qiu HN (2014) Proterozoic Fe-Cu metallogeny and supercontinental cycles of the southwestern Yangtze Block, southern China and northern Vietnam. Earth Sci Rev 139:59–82

Zhou Y, Duan QF, Chen YC, Tang JX, Cao L, Peng SG, Gan JM (2016) C, O, H, S, Pb and Sr isotope constraints on the metals sources of Huayuan Pb-Zn deposit in western Hunan Province. Acta Geol Sinica 90:2786–2802 ((**in Chinese with English abstract**))

Zhou JX, Luo K, Wang XC, Wilde SA, Wu T, Huang ZL, Cui YL, Zhao JX (2018a) Ore genesis of the Fule Pb-Zn deposit and its relationship with the Emeishan Large Igneous Province: evidence from mineralogy, bulk C-O-S and in situ S-Pb isotopes. Gondwana Res 54:161–179

Zhou JX, Wang XC, Wilde SA, Luo K, Huang ZL, Wu T, Jin ZG (2018b) New insights into the metallogeny of MVT Zn-Pb deposits: a case study from the Nayongzhi in South China, using field data, fluid compositions, and in situ S-Pb isotopes. Am Mineral 103:91–108

Zhou JX, Xiang ZZ, Zhou MF, Feng YX, Luo K, Huang ZL, Wu T (2018c) The giant Upper Yangtze Pb-Zn province in SW China: reviews, new advances and a new genetic model. J Asian Earth Sci 154:280–315

Zhou JX, Meng QT, Ren HZ, Sun GT, Zhang ZJ, An Q, Zhou CX (2020) A super-large co-occurring (associated) germanium deposit discovered in the Huangsi anticline area, Guizhou Province. Geotect Metal 44:1025–1026 ((**in Chinese**))

Zhou JX, Yang DZ, Yu J, Luo K, Zhou ZH (2021) Ge extremely enriched in the Zhulingou Zn deposit, Guiding City, Guizhou Province, China. Geology in China 48:665–666 ((**in Chinese**))

Zhu ZY, Cook NJ, Yang T, Ciobanu CL, Zhao KD, Jiang SY (2016) Mapping of sulfur isotopes and trace elements in sulfides by LA-(MC)-ICP-MS: potential analytical problems, improvements and implications. Minerals 6:110

Zscheckel T, Kreher-Hartmann B, Rüssel C (2016) Structural investigations on iron containing natural Zincblende using EBSD. J Phys Chem Solids 92:19–25

Charbit M (Ed.) (2010) Digital signal and image processing using MATLAB (Vol. 666). John Wiley & Sons

Barrie CD, Boyce AJ, Boyle AP, Williams PJ, Blake K, Wilkinson JJ, Lowther M, McDermott P, Prior DJ (2009) On the growth of colloform textures: a case study of sphalerite from the Galmoy ore body, Ireland. J Geol Soc London 166(3):563–582.

Belissont R, Munoz M, Boiron MC, Luais B, Mathon O (2016) Distribution and oxidation state of Ge, Cu and Fe in sphalerite by μ-XRF and K-edge μ-XANES: insights into Ge incorporation, partitioning and isotopic fractionation. Geochim Cosmochim Ac 177:298–314